

Old Dominion University

ODU Digital Commons

Electrical & Computer Engineering Theses & Dissertations

Electrical & Computer Engineering

Summer 2006

An Adaptive Algorithm to Identify Ambiguous Prostate Capsule Boundary Lines for Three-Dimensional Reconstruction and Quantitation

Rania Yousry Hussein
Old Dominion University

Follow this and additional works at: https://digitalcommons.odu.edu/ece_etds



Part of the [Electrical and Computer Engineering Commons](#), and the [Theory and Algorithms Commons](#)

Recommended Citation

Hussein, Rania Y.. "An Adaptive Algorithm to Identify Ambiguous Prostate Capsule Boundary Lines for Three-Dimensional Reconstruction and Quantitation" (2006). Doctor of Philosophy (PhD), Dissertation, Electrical & Computer Engineering, Old Dominion University, DOI: 10.25777/p4bg-2k45
https://digitalcommons.odu.edu/ece_etds/85

This Dissertation is brought to you for free and open access by the Electrical & Computer Engineering at ODU Digital Commons. It has been accepted for inclusion in Electrical & Computer Engineering Theses & Dissertations by an authorized administrator of ODU Digital Commons. For more information, please contact digitalcommons@odu.edu.

**AN ADAPTIVE ALGORITHM TO IDENTIFY AMBIGUOUS
PROSTATE CAPSULE BOUNDARY LINES FOR 3D
RECONSTRUCTION AND QUANTITATION**

by

Rania Yousry Hussein

M.Sc. Computer Science, May 2000, Old Dominion University, USA

B.Sc. Computer Engineering, June 1997, Arab Academy for Science and Technology,
Egypt

A Dissertation Submitted to the Faculty of
Old Dominion University in Partial Fulfillment of the
Requirement for the Degree of

DOCTOR OF PHILOSOPHY

ELECTRICAL AND COMPUTER ENGINEERING

OLD DOMINION UNIVERSITY

August 2006

Approved by:

Frederic D. McKenzie (Director)

K. Vijayan Asari (Member)

R. James Swanson (Member)

Stephen A. Zahorian (Member)

ABSTRACT

AN ADAPTIVE ALGORITHM TO IDENTIFY AMBIGUOUS PROSTATE CAPSULE BOUNDARY LINES FOR 3D RECONSTRUCTION AND QUANTITATION

Rania Hussein
Old Dominion University, 2006
Director: Dr. Frederic McKenzie

Currently there are few parameters that are used to compare the efficiency of different methods of cancerous prostate surgical removal. An accurate assessment of the percentage and depth of extra-capsular soft tissue removed with the prostate by the various surgical techniques can help surgeons determine the appropriateness of surgical approaches. Additionally, an objective assessment can allow a particular surgeon to compare individual performance against a standard. In order to facilitate 3D reconstruction and objective analysis and thus provide more accurate quantitation results when analyzing specimens, it is essential to automatically identify the capsule line that separates the prostate gland tissue from its extra-capsular tissue. However the prostate capsule is sometimes unrecognizable due to the naturally occurring intrusion of muscle and connective tissue into the prostate gland. At these regions where the capsule disappears, its contour can be arbitrarily reconstructed by drawing a continuing contour line based on the natural shape of the prostate gland. Presented here is a mathematical model that can be used in deciding the missing part of the capsule. This model approximates the missing parts of the capsule where it disappears to a standard shape by using a Generalized Hough Transform (GHT) approach to detect the prostate capsule. We also present an algorithm based on a least squares curve fitting technique that uses a prostate shape equation to merge previously detected capsule parts with the curve equation to produce an approximated curve that represents the prostate capsule. We have tested our algorithms using three shapes on 13 prostate slices that are cut at different locations from the apex and the results are promising.

ACKNOWLEDGMENTS

First I heartily would like to acknowledge and express my thanks and gratitude to Allah, who granted me the ability and patience to start and complete this thesis.

I am very grateful to my advisor Dr. Rick McKenzie who has been supportive to me throughout my graduate studies and during the completion of this thesis. I very much appreciate his time, patience, understanding, guidance, and continual encouragement without which I would not have been able to complete my dissertation. Many thanks to Dr. Vijayan Asari who taught me the image processing course and to Dr. Stephen Zahorian who taught me the statistical pattern recognition course from which I gained important knowledge that helped me in my research. My thanks also go to Dr. Jim Swanson for his time and valuable input to this study. I thank them all for being my committee members and I appreciate their time and feedback.

Far too many people to mention individually have assisted in so many ways during my study and they all have my sincere gratitude. In particular, I would like to thank Dr Jose Diaz for helping me with the pathological part of my dissertation. Thanks to the staff of the interlibrary loan of ODU for their quick response to my requests. Many thanks to Hector Garcia and Mark Scerbo for the technical support I needed to run my experiments. Special thanks to Dr Sacharia Albin for his encouragement and friendly talks. Thanks to Linda Marshall for her friendly nature in handling office matters.

I sincerely wish to express my appreciation and thanks to my husband Hesham Anan for his valuable support and the great amount of time given to me in this endeavor. Without his sincere help, I would not have been able to finish my studies. I also owe a great debt to my beloved daughters Yomna and Aaya who have missed me in so many aspects of life during my studies. Special thanks to Yomna who accompanied me through my whole graduate studies and who supported me with her prayers and kind words. I also thank numerous other relatives and friends whose names do not appear here. I appreciate their support in the spirit of continuous friendship and for always being there when I needed them

No words will be enough to show my appreciation for the supportive will, generosity and love of my dear family. I am deeply grateful to my mother for her greatness and for always being my lifelong role model who paved the path for me with the lessons she had to learn before me. I thank my father for always reminding me that hard work and positive thinking will yield success. I sincerely thank my beloved sister Lamiaa for her great help and support during the final stages of this thesis, without which I would not have been able to make it to the defense at that time. My thanks also go to my brother Ahmed for his continual encouragement and for considering me his role model.

Finally, I would like to thank the one closest to my heart, if not in physical presence, the memory of my grandmother, who was a foundation of strength and inspiration for me.

TABLE OF CONTENTS

LIST OF TABLES	ix
LIST OF FIGURES	x
CHAPTER I.....	1
1 INTRODUCTION	1
1.1 Introduction.....	1
1.2 Motivation.....	3
1.3 Problem Definition.....	5
1.4 Approach.....	8
1.5 Thesis Organization	8
CHAPTER II.....	10
2 BACKGROUND	10
2.1 Introduction.....	10
2.2 Prostate anatomy	14
2.3 In vitro data and histology slides	16
2.4 Digitizing Microscopic Slides.....	17
2.5 Detecting Histological Patterns of Elastic Fibers within the Prostate Capsule	18
2.6 Texture Analysis	20
2.6.1 Structural Methods.....	21
2.6.2 Mathematical Morphology.....	22
2.6.3 Model-based Methods.....	23
2.6.4 Transform methods	23
2.6.5 Statistical Methods.....	23
2.6.6 Texture analysis in medical imaging	25
2.7 Medical image segmentation	25
2.7.1 Thresholding	26
2.7.2 Region-growing	26

2.7.3	Artificial Neural Networks (ANNs).....	28
2.7.4	Deformable models.....	29
2.7.5	Generalized Hough transform.....	32
CHAPTER III		35
3	RELATED WORK.....	35
3.1	Introduction.....	35
3.2	Two-dimensional Prostate Boundary Detection from Ultrasonographic Image...	36
3.2.1	Edge-Based Detection Methods.....	36
3.2.2	Texture-Based Detection Methods	37
3.2.3	Model-Based Detection Methods	38
3.3	Discussion.....	41
CHAPTER IV		43
4	ESTIMATION OF THE PROSTATE CAPSULE USING SHAPE INFORMATION.....	43
4.1	Introduction.....	43
4.2	Detecting Histological Patterns of Elastic Fibers within the Prostate Capsule	43
4.3	A Mathematical model for a standard prostate shape top down anterior to posterior	46
4.4	Approach.....	50
4.4.1	Generalized Hough Transform (GHT) shape algorithm.....	51
4.4.2	The least squares shape algorithm	53
4.4.3	Curve Adjustment Algorithm	57
4.5	Summary.....	58
CHAPTER V		59
5	IMPLEMENTATION AND EXPERIMENTAL RESULTS.....	59
5.1	Images preprocessing.....	59
5.2	Test bed.....	60
5.3	Testing.....	62

5.3.1	Testing Least squares algorithm	64
5.3.2	Testing GHT algorithm.....	72
5.4	Performance evaluation	78
5.5	Discussion.....	84
CHAPTER VI.....		86
6	CONCLUSION AND FUTURE WORK	86
6.1	Conclusion	886
6.2	Future Work.....	88

LIST OF TABLES

Table 1 A lookup table for the proposed GHT.	51
Table 2 Test bed.....	60
Table 3 Detailed steps of applying least squares algorithm on a slice.....	64
Table 4 Results of running the least squares algorithm on RP38mm30 using circle equation.....	68
Table 5 Results of running the least squares algorithm on RP38mm30 using ellipse equation.....	69
Table 6 Least squares algorithm results after the 2 nd run.....	70
Table 7 Detailed steps of applying GHT algorithm on RP38mm30.....	73
Table 8 Results of running the GHT on RP38mm30 using circle equation.	75
Table 9 Results of running the GHT on RP38mm30 using ellipse equation.....	76
Table 10 GHT results after the 2 nd run.....	76

LIST OF FIGURES

Fig 1. A prostate slice with the hand-drawn boundary.	6
Fig 2. Prostate anatomy.....	7
Fig 3. Prostate Anatomy.	14
Fig 4. Prostate orientation within the human body.....	15
Fig 5. Epithelial cells and parenchymal contour.....	15
Fig 6. The prostate Capsule	16
Fig 7. Histological wavy patterns of the prostate capsule as seen under microscope with a) 4x, b)10x, and c)40x magnification.....	19
Fig 8. histological wavy patterns of prostate capsule can not be seen when scanned with a 1200 ppi flatbed scanner	19
Fig 9. Histological wavy patterns of prostate capsule were detected under 20x magnification using scanscope system of Aperio Technologies	20
Fig 10. Texture Analysis Taxonomy	21
Fig 11. Illustration of region growing.....	27
Fig 12. The structure of a typical back-propagation ANN.	28
Fig 13. An illustration of GHT parameters and lookup table	33
Fig 14. A prostate slice with parenchymal contour (inner line), slice perimeter (outer line), and the prostate capsule (dashed line).	44
Fig 15. A standard prostate shape.	46
Fig 16. A standard shape of a prostate slice.....	48
Fig 17. Limacon curves (a) when $a < b$, (b) when $a < b < 2a$, and (c) when $2a \leq b$	50
Fig 18. Least squares method and prostate shape equation. (a) Arrows point to the detected parts of the prostate capsule, (b) Arrow points to the curve representing the prostate shape located as close as possible to the capsule parts.	55
Fig 19. New shape curve after merging the capsule parts into the original shape curve..	55
Fig 20. Shape curve extending beyond the prostate perimeter.	57
Fig 21. Contours.....	58
Fig 22. Slice Image.	59

Fig 23. Limacon curve generated for two different slices.	63
Fig 24. Manual marking of the capsule parts that are present in the slice.	64
Fig 25. Root Mean Square Error for the least squares algorithm.	79
Fig 26. Root Mean Square Error for the GHT algorithm.	80
Fig 27. Thresholds with respect to an actual slice image.	81
Fig 28. %matching for least squares algorithm.	82
Fig 29. %matching for GHT algorithm.....	84

CHAPTER I

INTRODUCTION

1.1 Introduction

Prostate cancer is the most common form of cancer among men in the United States. The American Cancer Society estimated that about 30,350 men would die of prostate cancer disease from a total of 232,090 new cases in 2005 [1]. Prostate specific antigen (PSA) test in conjunction with annual digital rectal exams (DRE) have made early diagnosis possible and can help physicians better assess the extent of the disease and its effect on surrounding organs.

Removing a sample of tissue from the patient and sending it to a pathologist for examination, however, is still the norm for diagnosing many cases of cancer. This procedure is called a biopsy and is currently the gold standard for diagnosing prostate cancer. Although such diagnosis is sometimes straightforward, there are several challenges remaining. Perhaps the greatest challenge is that prostate cancer is generally multifocal and only a very tiny portion of the prostate is sampled. Traditional biopsy sampling procedures use 6 parallel core samples, while newer procedures take 8-32 core biopsy samples [11]. Although the optimal number of biopsy samples remains unclear, the overall strategy of increasing the number of samples reduces errors on histopathologic grading and improves cancer detection and risk assessment. There has been a significant amount of research regarding optimizing biopsy protocols to increase the likelihood of detecting prostate cancer according to certain objective and quantitative criteria. The hope is that with optimized protocols one could achieve improved detection rates with fewer needles. An even better method would be to rely solely on imaging techniques, thus sparing the patient from painful and inconvenient procedures.

The journal model for this dissertation is the IEEE/ACM Transactions on Networking.

Imaging modalities are used to aid in the detection and clinical staging of prostate cancer. Transrectal Ultrasound (TRUS) is the most frequently used imaging technique in cancer detection. It is used in needle biopsy procedures to provide a high-resolution image of the prostate and thus enables more accurate needle placement and tissue sampling. It provides a good estimate of the prostate volume, but it has a low sensitivity overall and its specificity for malignant versus benign tumors varies. In addition to TRUS, Computed Tomography (CT) and Magnetic Resonance Imaging (MRI) are widely used in determining the stage of the cancer and its extent. However, images produced by CT and MRI have low tissue contrast and low signal-to-noise (SNR) ratio. Unfortunately, no imaging modality can effectively differentiate cancerous tissues from normal tissues, making their overall accuracy in detecting and diagnosing prostate cancer low.

As far as treatment is concerned, the options for local therapy have proliferated and include various forms of radiation delivery, cryo-destruction, and such novel forms of energy delivery as in high-intensity focused ultrasound. Surgical removal, however, remains the standard procedure for cure. Although surgical prostatectomy is currently the norm, there are few objective parameters used to compare the efficiency of each form of surgical removal. As surgeons apply these different surgical approaches, a quality assessment would be most useful, not only with regard to overall comparison of one approach versus another, but also a surgeon's evaluation of personal surgical performance as related to a standard. Parameters such as the percent of capsule covered by soft tissue and, where present, the average depth of soft tissue coverage can be used to compare the efficiency of one form of surgical removal with another.

The objective of this research is to facilitate and provide a more accurate and objective assessment of the percentage and depth of extra-capsular soft tissue removed with the prostate by the various surgical approaches. Assessment accuracy, determination time, and cost will be improved by developing a software algorithm to perform automatic recognition of the prostate capsule, a process that pathologists are tediously doing.

1.2 Motivation

Currently there are few objective parameters that are used to compare the efficiency of one form of prostate surgical removal over another. An objective methodology that could be applied to surgical specimens would be of immense value to establish clinical trial criteria for skills assessment, for trial entry, for ongoing assessment during trial conduct, and finally for dissemination of a mechanism of quality control and reassessment of individual surgical practices.

A novel methodology to computerize and objectively quantify the assessment process is to utilize a 3D reconstructed model for the prostate gland. With such a model, the curvature of the capsule, the irregular borders of the extra-capsular tissues, as well as the extensions of the tumor can be visualized. Subsequently, software algorithms may be designed and applied to quantify the virtual model.

In general, the reconstruction process consists of three main steps: a) extracting the object contours, b) interpolating intermediate contours, and c) reconstructing surfaces or volumes. During the last decade, there has been a considerable amount of research in the visualization and 3D reconstruction of medical data. Most research focused on developing or improving algorithms that consider the last two steps of the reconstruction process. Identifying and outlining objects in medical images, however, is an important task for many applications (a task for which the human eye is well equipped and experts are well capable of doing manually). Besides the fact that manual delineation of objects from large image sets is a time-consuming and a tedious procedure, it is also sensitive to an expert's bias or experience.

Researchers have long investigated automatic algorithms for contours extraction of the prostate from medical images of different modalities especially in ultrasound images. Aarnik et al. [2] reported a scheme for prostate recognition in ultrasonographic images based on a nonlinear Laplace filtering edge detection technique. An edge intensity image was obtained using edge strength and location information. The detected edges are linked, and a knowledge database of prostate shape is incorporated using edge-linking algorithms to construct a complete boundary of the prostate. Liu et al. [40] reported a segmentation scheme for prostate edge

detection from ultrasound images. Their scheme is dependent on image quality and produces partial edge information rather than a complete prostate boundary. These attempts have had limited success due to large variability of prostate shapes, considerable amount of noise in images, low contrast between prostate and non prostate regions, and the incompleteness of prostate contour in some images. Accordingly, these algorithms are not in wide use although they have a certain degree of clinical utility.

Some researchers have employed neural networks and texture features to automatically identify the prostate boundaries. Prater and Richard [62] developed four different three-layer neural networks to classify prostatic and non prostatic tissue in transrectal ultrasound images. Their study showed that extensive trial and error is required to find the best number of nodes in each layer for the best results. In addition, the desire to use large training sets for effective network training makes the preparation of training patterns a tedious and time consuming task. Richard and Keen [68] presented a pixel classifier based on four texture energy measures associated with each pixel in ultrasound prostate images. Their study, however, showed an extensive computation and unpredictable number of produced classes. In an attempt to avoid the limitations that other researchers had faced with their algorithms, Pathak et al. [56] presented a new paradigm for the edge-guided delineation of the prostate in ultrasound images. The image contrast was enhanced and the speckle noise was reduced and the resulting image was further smoothed. A priori knowledge of the prostate shape and echo pattern was finally used to detect the most probable edges of the prostate. However, the algorithm-detected prostate edges were provided to the user as a visual guide to manually link them which would subject the results to observer bias.

Despite the numerous research studies in segmenting structures from medical images and reconstructing a compact geometric representation of these structures, no study, to the best of our knowledge, has been done to automatically identify the prostate capsule in medical images. Identifying prostate capsule is essential in staging prostate cancer and it greatly affects the treatment options. Studies have shown that

the presence of metastases in the prostate's adjacent organs is highly related to their penetration to the prostate capsule, which therefore influences the prognosis after surgical and hormonal treatment [50]. In addition to its importance in prostate prognosis, automatically identifying the prostate capsule provides a more accurate and objective assessment of the percentage and depth of extra-capsular soft tissue removed with the prostate by the various surgical approaches. Not only does this assessment allow surgeons to compare the quality of one surgical approach versus another, it also provides an evaluation of surgeons' surgical performances as related to a standard [49].

1.3 Problem Definition

The objective of this research is to facilitate and provide a more accurate and objective assessment of the percentage and depth of extra-capsular soft tissue removed with the prostate by various surgical approaches. Visualization methods and tools were developed for images of prostates slices that are provided by the Pathology department at Eastern Virginia Medical School (EVMS) [49]. The visualization tools interpolate and present 3D models of prostate specimens upon which measurement algorithms are applied to determine statistics about extra-capsular tissue coverage. The contour of the gland (the capsule) had to be manually outlined by a pathologist on each slice's image to enable construction of the 3D models of the prostate gland and the extra-capsular tissue. Besides the fact that manual outlining of the capsule is tedious and sensitive to observer bias and experience, it is considered a significant source of error in the assessment accuracy of the percentage of extra-capsular soft tissue [49]. The reason is that the thickness of the hand drawn line is approximately 0.046 inches (1.168 mm) [49], which makes deciding whether to consider its inner or outer edge contour an issue. If the inside edge is considered, then the boundary that separates the prostate capsule from the extra-capsular tissue (which will be referred to as 'fat') might be under-estimated, while considering its outer edge might over estimate the capsule. Manual outlining can also affect the accuracy of thickness calculations of the extracapsular tissue with respect to the capsule.



Fig 1. A prostate slice with a hand-drawn boundary.

The prostate gland sits right below the bladder and is wrapped around the urethra. Figure 2 is a transverse view of the prostate gland taken from a slice orthogonal to the urethra. A slice taken in this manner frequently reveals a distinctive chestnut or apple shape to the prostate. The sometimes distinctive arrow shape of the urethral wall can be seen in the center of the slice. The prostatic glandular epithelial elements are part of the prostate gland and they are the histological compartments where cancer originates (Fig. 2). Later, we will discuss the use of an imaginary line surrounding those glandular elements which we will call the parenchymal contour.

In order to automatically identify the contour of the gland within each prostate slice and replace the arduous and costly manual process, a software algorithm will need to be developed that recognizes the prostate gland capsule utilizing these elements of anatomy and shape.

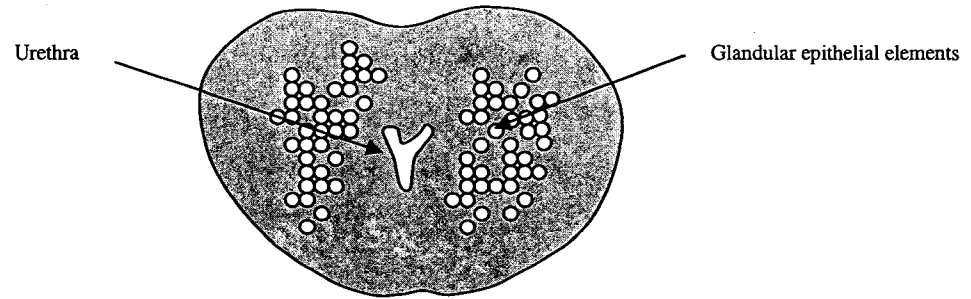


Fig 2. Prostate anatomy.

Certain anatomical features make capsules generally detectable; however, the prostate capsule is unrecognizable in some areas because of the naturally occurring intrusion of muscle into the prostate gland at the anterior apex and fusion of extraprostatic connective tissue with the prostate gland at its base. At these regions where the prostate capsule disappears, its contours will need to be reproduced by drawing a continuing contour line from those areas where the capsule can be objectively recognized based on the natural shape of the prostate gland.

To the best of our knowledge, we are unaware of any research that automatically detects the prostate capsule; however some efforts were reported in literature to detect the prostate boundary that separates the prostate from the surrounding body organs. Some researchers have used edge-based boundary detection methods that locate edges that correspond to local peaks in the intensity gradient of an image [56], while others used texture-based methods that characterize regions of an image on the basis of measures of texture [68]. The reader can refer to [76] for a review of the current prostate boundary detection techniques in ultrasound images. Although edge detection and texture recognition techniques have been used for the automatic delineation of prostate boundary, determining the prostate capsule cannot be completely solved by only applying such clean cut techniques. This is because the capsule detection depends on many factors such as recognizing the histological pattern of the elastic and collagenous fibers within the prostate capsule, urethra location, parenchymal contour location, as well as the whole shape.

Thirteen specimens of radical prostatectomies were used for our study. The prostate slices were prepared using the whole mount technique where a prostate specimen was received fresh, was measured craniocaudally, antero-posteriorly and transversely, weighed, and then dipped in water to determine its volume. The whole specimen was inked blue on the right side and red on the left to avoid any possible flipping of the slices while scanned. The specimen was then serially cut into 5-8 slices from apex to base at relatively precise and parallel 5 mm intervals in a perpendicular angle to the urethral apical orifice.

1.4 Approach

We present two approaches that use shape information to estimate the prostate capsule based on previously recognized collagenous fibers that uniquely identify the capsule of the prostate tissue. The first approach uses Generalized Hough Transform (GHT) technique in conjunction with a mathematical model that represents a standard shape for the prostate slices at different locations from the apex. The GHT has been used in literature to globally detect irregular shapes in images and has proved successful in many applications [83], [20][63]. The other approach is based on a least squares curve fitting technique that uses a prostate shape equation to merge the previously detected capsule parts with the curve equation to produce an approximated smoothed curve that represents the prostate capsule. The least squares method is a very popular technique used to compute estimations of parameters and to find the best fitting model for discrete data. It is widely used in literature to fit a function (which may represent a certain shape) to a set of data which can be used in many applications including medical imaging [59].

1.5 Thesis Organization

The rest of the thesis is organized as follows:

Chapter 2- Background: In chapter 2, we present the background in histopathologic imaging, texture analysis and image segmentation techniques.

Chapter 3- Related Work: In chapter 3, we present the research efforts in the field of image segmentation and discuss the pros and cons of each method and how related each method is to our problem.

Chapter 4: Estimating the prostate capsule using shape information: In chapter 4, we explain our proposed approaches in details.

Chapter 5: Experimental Results: In chapter 5, we present our experimental results from running the 2 proposed approaches on our test bed that consists of 13 different prostate slices cut between 5 to 30mm from the apex. Our performance evaluation is based on calculating percentage of deviation from the expected capsule as well as calculating the Root Mean Square Error RMSE.

Chapter 6: Conclusion and future work: Finally, in chapter 6, we present the contributions of our research and provide suggested future work.

CHAPTER II

BACKGROUND

2.1 Introduction

In the past years, imaging procedures have changed medical practice so fundamentally that not only are they indispensable, but it is simply impossible to imagine medical practice without them. Medical imaging is the most important source of anatomical and functional information, which are indispensable for up-to-date diagnosis and therapy. It is increasingly being used for a tremendous number of medical applications. Some of these applications include but are not limited to: pre-operative imaging and image guided surgery.

Pre-operative imaging provides three-dimensional information about anatomy, function and the location of both diseases and healthy structures. Prior to the patient's surgery, image scans are usually taken and transferred to tape or optical disc to be read by the system's computer during surgery. Pre-operative imaging decreases or eliminates the need for intraoperative x-rays thereby sparing the patient and surgeon radiation exposure. Reviewing the patient's x-rays, CAT Scans, and/or MRI studies helps the surgeon to visualize the surgical process in his mind. Preoperative imaging thus helps surgeons perform complex reconstructions safer and faster.

Image-guided surgery techniques rely on a powerful computer system, which assists the surgeon in precisely localizing a lesion, in planning each step of the procedure via a 3D model on the computer screen, and in calculating the ideal access to a tumor before the operation. The tumor and its surroundings can be viewed from different angles and in relation to landmark structures, such as the optic nerve or the brain stem. This technique has been employed in neurosurgery since the mid-1990s.

While in the past, images were typically 2D; there has been a shift towards reproducing the three-dimensionality of human organs. 3-D Visualization generally refers to transformation and display of 3-D objects so as to effectively represent the 3D nature of the objects. The goal of visualization in biomedical computing is to formulate and realize a rational basis and efficient architecture for productive use of

biomedical image data. The need for new approaches to image visualization and analysis will become increasingly important as improvements in technology enable more data of complex objects and processes to be acquired. Visualization has been used in many clinical and biological applications. One of the important clinical applications of 3-D visualization is virtual endoscopy, which is the navigation of a virtual camera through a 3D reconstruction of a patient's anatomy enabling the exploration of the internal structures to assist in surgical planning. A virtual endoscopy tool can be used so that the surgeon can visualize the 3D model of an anatomical structure and define a trajectory path inside the model in order to perform a virtual exploration. When the virtual camera flies through the model, the surgeon can track the position of the virtual camera inside the model on one screen, view what the endoscopic camera sees on another screen and track the position of the camera on 2D slices. Virtual exploration through patient-specific data can help the surgeon perform a diagnosis without having to operate on the patient. Virtual endoscopy (VE) is an integration of medical imaging and virtual reality technologies, leading to a computer-based alternative to the traditional fiberoptic endoscopy for examining the interior structures of human organs. It has many advantages as compared to traditional endoscopy procedures, such as being non-invasive, cost-effective, highly accurate, free of risks and side effects, and easily tolerated by the patient. Virtual endoscopy has been under development in many clinical areas, such as virtual colonoscopy, virtual bronchoscopy, virtual angiography, virtual cystoscopy, virtual laryngoscopy, virtual myelography and others. Continual advancement of VE technologies shall have a great impact for computer applications in medicine.

Another application for visualization can be found in neurosurgery, where detecting and locating brain tumors are very critical. Visualization in order to pre-operatively assess and guide surgical operations has been used successfully and increasingly over the past two decades. Neurosurgery is a complex procedure, involving extended knowledge and understanding of complicated relationships between normal anatomy and pathology. Patients with tumors undergo multimodality image scanning preoperatively to help the neurosurgeon understand the anatomy of interest. Different scans can be co-registered in order to produce single visualizations

of complementary information, where in the registration process each point in one image is mapped onto the corresponding point in another image. The surgeon can then use this information to more carefully plan the surgical approach and determine the margins of pathology with respect to cerebral vasculature and eloquent cortical tissue.

Imaging technologies are very important in visualizing 3-D anatomies, which is the key step in 3-D reconstruction. Magnetic Resonance Imaging (MRI) is an imaging technique used primarily in medical settings to produce high quality images of the inside of the human body. It is based on the magnetization of water molecules, which are present in different concentrations in most types of tissue in the body. This makes the method particularly well suited to the visualization of soft tissue, as bones give off nearly no signal and are therefore almost invisible. This method is used primarily to visualize various types of tumors, internal organs such as the brain and the liver, and other organs that are otherwise barely visible, such as ligaments. Disadvantages of MRI are its high cost, the complexity of its equipment, and the requirement for the patient to remain still in the magnet for about half an hour, and the problems associated with the presence of high magnetic fields. Computed Tomography (CT), sometimes called CAT scan, uses special x-ray equipment to obtain image data from different angles around the body, and then uses computer processing of the information to show a 2D cross-section of body tissues and organs. A 3D image can be then reconstructed from a series of 2D cross sectional images. CT imaging is particularly useful because it can show several types of tissues, bones, and blood vessels with great clarity. Using specialized equipment and expertise to create and interpret CT scans of the body; radiologists can more easily diagnose problems such as cancers, cardiovascular disease, and infectious diseases. It provides detailed, cross-sectional views of all types of tissue. It is often the preferred method for diagnosing many different cancers, including lung, liver, and pancreatic cancer, since the image allows a physician to confirm the presence of a tumor and to measure its size, precise location, and the extent of the tumor's involvement with other nearby tissue. CT can clearly show even very small bones, as well as surrounding tissues such as muscle and blood vessels. CT examinations are fast and simple especially in trauma cases;

they can reveal internal injuries and bleeding quickly enough to help save lives. CT scanning is painless, noninvasive, and accurate. Diagnosis made with the assistance of CT can eliminate the need for invasive exploratory surgery and surgical biopsy. CT does involve exposure to radiation in the form of x-rays, but the benefit of an accurate diagnosis far outweighs the risk. The risk of serious allergic reaction to iodine-containing contrast material is rare. The algorithm that will be developed in this research should be applicable to MRI images as well as CT images since both of these techniques can be used to obtain prostate images.

Three-dimensional reconstruction has led to the formation of 3-D physical biomodels, which greatly facilitates characterization, analysis and simulation of tissue structures. 3-D imaging and visualization methods are emerging as the method of choice in many clinical examinations, replacing some previously routine procedures, and significantly complementing others. The continuing evolution of 3-D and visualization imaging promises even greater capabilities for accurate noninvasive clinical diagnoses and treatment, as well as for quantitative biological investigations and scientific exploration, targeted at ever increasing the understanding of the human condition and how to improve it. In the near future, 3-D imaging will be integrated in surgical suites with imaging instrumentation, which will allow surgeons to probe tissue intra-operatively and view detailed soft-tissue anatomy in real time while performing interventional procedures.

This research is involved in another important application for prostate cancer surgery where cancerous prostates are surgically removed. There is a need for improved non-invasive pre-operative techniques that can more accurately measure tumor volume and extent, and thereby more clearly indicate the need for surgery. The ability to visualize the prostate capsule and tumor in relationship to the complicated anatomic structures in this region, including the neurovascular bundles and seminal vesicles, is helpful to preoperative planning of surgical approaches to tumor resection. Therefore a procedure that can provide a marker for pre-surgical stage can improve the outcome of necessary surgeries. This research works towards a process for automatically delineating the prostate gland capsule post excision but may one day contribute to a more accurate in-vivo approach.

2.2 Prostate anatomy

The prostate gland is a chestnut-sized structure that is located in front of the rectum, below the bladder, and surrounding the urethra. Anatomically, the prostate is divided into peripheral, central, and transitional zones. In a normal prostate, the peripheral zone constitutes approximately 65% of the prostatic volume [86], where the prostate's posterior, lateral, and apical regions are found. The cone-shaped central zone comprises approximately 25% of the prostate [86], and it surrounds the ejaculatory ducts. The transition zone consists of two lobes that surround the proximal urethral segment laterally and anteriorly and it comprises from 5 to 10% of a normal prostatic volume [86]. The peripheral zone is the most frequent place of prostate cancer from which about 70% of prostate cancers originate [75].

Fig 3 shows the basic anatomy of the prostate and Fig 4 shows its parts and orientation within the human body.

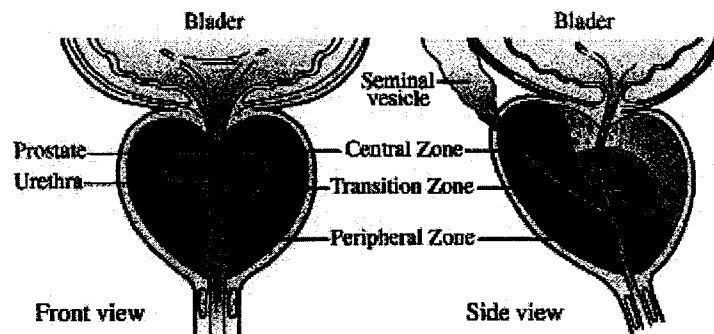


Fig 3. Prostate Anatomy¹.

¹ Figure from [86] Fig. 1. Zonal anatomy of the prostate. (Copyright © (2002) Prostate Research Campaign UK. Reproduced with permission from Kirby, R.S., 2002. *The Prostate: Small Gland, Big problem*, second ed. Prostate Research Campaign, London, UK.)

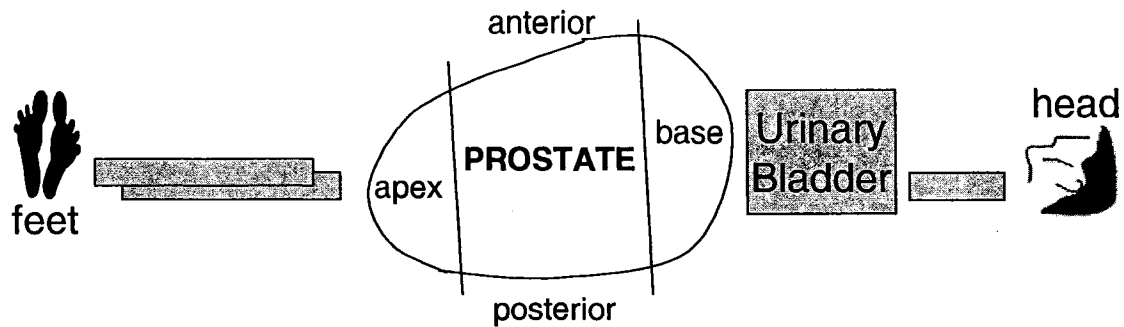


Fig 4. Prostate orientation within the human body.

The prostate tissue comprises a number of tissue subtypes, the most important of which are the epithelial cells (glandular tissue) and the capsule. The epithelial cells are the histological compartments where cancer originates. Fig 5 shows the epithelial cells surrounded by a thin virtual contour called parenchymal contour. The main goal of a prostatectomy is to remove the whole gland, particularly its epithelial elements, to avoid a significantly increased risk for positive tumor margins.

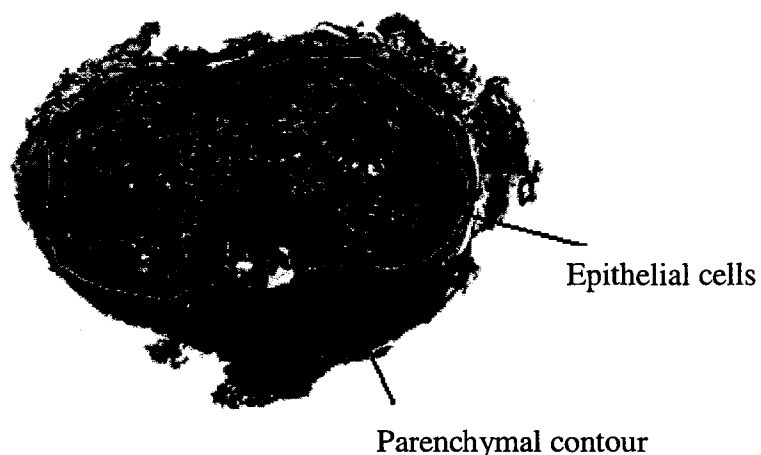


Fig 5. Epithelial cells and parenchymal contour.

The prostate capsule is a fibromuscular band of transversely oriented collagenous fibers, and it lies between the parenchymal contour and the periprostatic tissues (Fig 6).

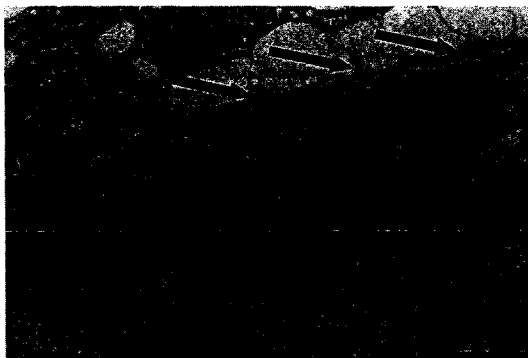


Fig 6. The prostate Capsule.

Studies have shown that the prostate capsule has a mean thickness of 0.5 to 2 mm [72], however it is incomplete at the apex and is difficult to determine at the base [72], [50], and [6]. This is due to the naturally occurring intrusion of muscles into the prostate gland at the anterior apex, and fusion of extraprostatic connective tissue within the prostate gland at its base. While detecting the prostate capsule may be subjective in certain areas, the recognition of the parenchymal contour is unequivocal and objective.

2.3 In vitro data and histology slides

After the prostate is removed surgically, it is measured craniocaudally, anteroposteriorly and transversely. It is weighed and immersed in water to determine its volume. The whole gland is then inked blue on the right and red on the left to label the surgical margins. A posterior midline is inked with a black ribbon running from base to apex and the dipped in Bowin's solution to fix the ink. The prostate is then fixed in formalin for 24 hours for "whole mount" processing and for histopathological review. After that it is serially cut from apex to base at precise and parallel 5 mm

intervals in a perpendicular angle to the urethral apical orifice. The sections are then submitted in large cassettes and processed in a tissue processor (Tissue Tek VIP Model 52150460) overnight, then embedded in paraffin (Tissue Tek Embedding center Model 4603). The paraffin blocks are cut with a sliding microtome (Leica Sliding Microtome Model SM2000R). Sections of four microns in thickness are then mounted on large glass slides, stained with Eosin and Hematoxylin and coverslid [73].

2.4 Digitizing Microscopic Slides

In pathology, tissue samples are processed and made into stained tissue sections to be mounted on glass slides for interpretation. Representing the histological features of a slide in digital formats may require using a very high resolution capturing device that can capture the details of the tissue as seen under a microscope. Spatial resolution is a term that refers to the number of pixels that construct a digital image. As the image's spatial resolution increases, the number of pixels that can digitize it increases. The number of pixels contained in a digital image and the distance between every two pixels (known as the sampling interval) determine the accuracy of the digitizing device. Optical resolution measures the ability of a microscope to reveal the details present in a specimen. It is related to the number of pixels in the digital image (spatial density), optics' quality, and the microscope's sensor and electronics. The value of each pixel in the digital image represents the intensity of the optical image averaged over the sampling interval. According to Nyquist sampling theorem, a sampling interval that is greater than twice the highest specimen spatial frequency is needed to accurately digitize a microscope specimen without losing any details available to the human eye. Details with high spatial frequency will not be accurately represented in the final digital image if sampling of the specimen occurs at an interval beneath that required by the Nyquist sampling theorem. In optical microscopes, the Abbe limit of optical images' resolution is 0.22 micrometers ($0.22 \times 40 = 8.8$ micro inches). This means that a digitizer must be capable of sampling at intervals that correspond to 0.11 micrometers (4.4 micro inches) or less in the specimen space.

Digital images can be generated by a scanner or by a digital camera. The most common way of digitizing medical images is with a microscope equipped with a

digital camera and a robotic stage to capture thousands of individual images. Once acquired, these images must be stitched (or tiled) together to form the final representation of the slide. This process can result in the misalignment of images due to their large numbers; besides, it is very time consuming for pathologists.

The best alternative solution is to produce an image of the entire microscopic slide, thereby producing a true digital representation of the entire histopathological specimen. Accordingly, very high-resolution scanners should be used in order to capture the fine details of specimens. As previously mentioned, the Nyquist theorem requires that a minimum of two pixels should be used to cover the corresponding limiting resolution distance, so that all of the specimen information available to the human eye is captured. This means that a scanner is needed that can scan at pixel resolutions of 4.4 micro inches (0.11 micrometers) or smaller to meet the limiting resolution distance of the optical microscope. A scanner with 1200 ppi (pixels per inch) will only scan at 416 micro inches ($1200 \times 2 = 2400$ to satisfy Nyquist, then samples that are spaced $1/2400 = 416$ micro-inches will be taken) resolution, which is considered very low compared to the 4.4 micro-inches resolution.

To the best of our knowledge, no such scanner is available on market that can scan at 0.11-micrometer pixel (about 113,000 pixels/inch) resolution but a close resolution was achieved by some systems like the scanscope developed by Aperio technologies. Scanscope can scan at 0.5 $\mu\text{m}/\text{pixel}$ (50,000 pixels/inch) at 20x magnification, and can scan at 0.25 $\mu\text{m}/\text{pixel}$ (100,000 pixels/inch) at 40x magnification.

2.5 Detecting Histological Patterns of Elastic Fibers within the Prostate Capsule

In this section, we will show images of a prostate slice scanned at different resolutions aiming to detect the histological patterns of elastic fibers within the prostate capsule. Fig 7 shows the prostate capsule fibers as seen under the microscope. The images were taken by Nikon CoolPix800 digital camera with resolution 1600x1200 ppi and were mounted to a Nikon compound light microscope. As seen from the figure, more details can be revealed by increasing the magnification. The histological wavy pattern can be marginally detected at 10x, clearly detected

under 40x magnifications, but can not be detected at 4x. However, it will require tiling a lot of captured sections to obtain a whole image of a prostate slice, which may cause misalignment of the different sections of the images.

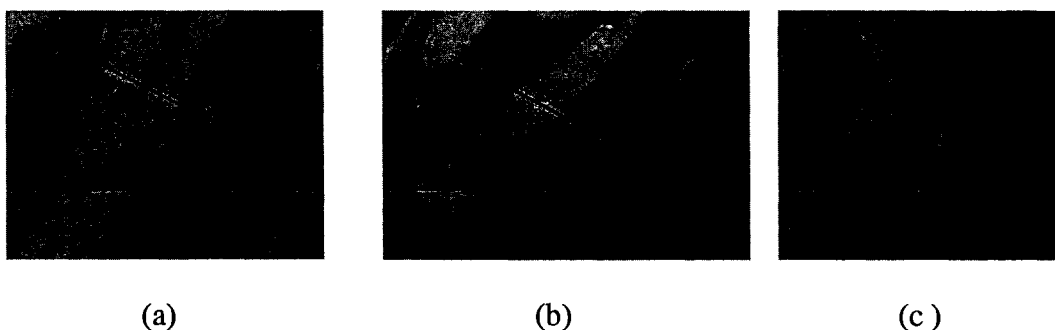


Fig 7. Histological wavy patterns of the prostate capsule as seen under microscope with a) 4x, b)10x, and c)40x magnification.

We have also scanned a microscope slide with a flatbed scanner with 1200x1200 ppi and were not able to detect the capsule with this resolution (Fig 8).

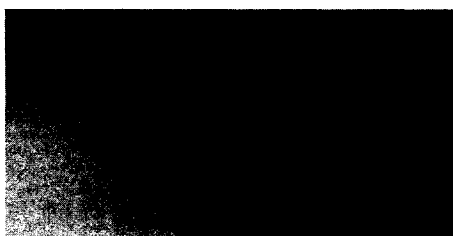


Fig 8. Histological wavy patterns of prostate capsule can not be seen when scanned with a 1200 ppi flatbed scanner.

We have tried the scanscope system developed by Aperio Technologies where microscope slides were scanned at 20x magnification. The histological wavy pattern was clearly detected as seen in Fig 9.



Fig 9. Histological wavy patterns of prostate capsule were detected under 20x magnification using scanscope system of Aperio Technologies.

From Fig 7 and Fig 8, we conclude that a resolution of 1200 or 1600 ppi with magnification between 20x and 40x should be acceptable; however, significant storage and processing power is still required.

2.6 Texture Analysis

The development of automated systems to analyze histopathologic images has been lagging due to the inherent difficulties in microscopy images. Uneven illumination, instrumentation noise, and improper specimen preparation are some of the artifacts in histopathologic images. Additionally, the overlapping cell boundaries resulting from the compact arrangements of cells exhibit a very low and uneven gradient magnitude that is difficult to recognize by traditional image processing algorithms such as edge detectors and region growing. Nowadays, however, the automated analysis of histopathologic images becomes possible owing to the advancements in imaging technologies and image processing systems.

Texture plays an important role in the perception of histological scenes and is used mainly to achieve image segmentation. It quantifies image properties such as smoothness, coarseness, and regularity by measuring the variation of the image intensity. According to Materka et al [47] and Castellano et al [12], approaches to texture analysis are categorized as structural, model-based, transform, and statistical methods (Fig 10).

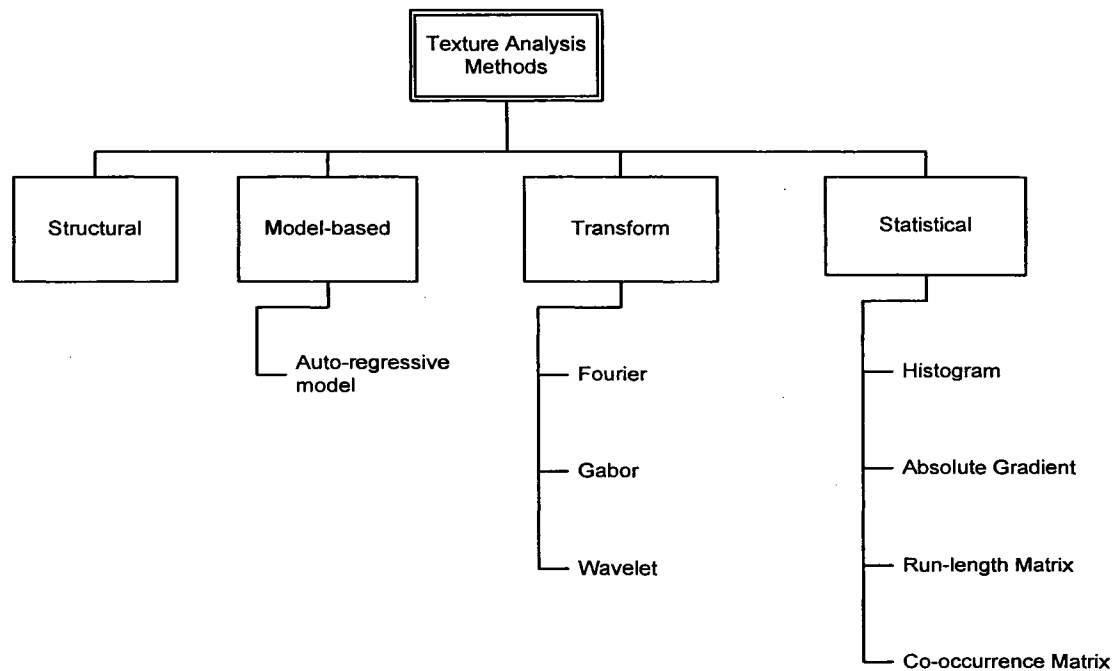


Fig 10. Texture Analysis Taxonomy.

2.6.1 Structural Methods

In structural methods [31], texture is represented by well-defined primitives (such as straight lines) and by placement rules (location) of those primitives.

Although they provide a good symbolic description of the image, structural methods are useful for image synthesis rather than analysis. The abstract description can not well define natural textures because of the variability of micro- and macrostructures where no clear distinction between them is available. Mathematical morphology is a more powerful tool for structural texture analysis.

2.6.2 Mathematical Morphology

Mathematical morphology, originally developed by Serra [74], is a set theory that uses set transformations (erosion and dilation) to extract the impact of a particular shape on images via structuring elements that encode primitive shape information. The structuring element is typically a circular disc, but it can be any shape.

There are many applications in which mathematical morphology was used in the analysis of texture in medical images. Samarabandu et al. [71] used fractal analysis based on mathematical morphology to detect trabecular bone structures in a radiograph of a rat femur. Their study showed promise in finding the degradation of bone structures, which can be a useful indicator for an early staged osteoporosis disease. Sutherland and Ironside [79] developed a novel image processing system which can segment images of human cerebellar tissue using morphological functions. Individual cells were linked together using a dilation function followed by an erosion, to form a region that represents the granular area. Zana and Klein [85] presented an algorithm based on mathematical morphology and curvature evaluation for the detection of vessel-like patterns in angiographic images. Mathematical morphology was well adapted to the tree-like geometry of vessels which they defined as bright patterns, piecewise connected, and locally linear. Marghani et al. [46] presented a morphological approach based on the shape for an automated method to identify cancer and normal colon tissue glands. The authors reported that using morphological operations based on structure elements can lead to better segmentation, and thus improve automation systems.

Mathematical morphology provides a quantitative description of geometrical structures using small patterns (structuring elements) of varying size and shape. It can

provide boundaries of objects and their skeletons and can be useful in edge thinning and pruning techniques. It is, however, unable to capture all the meanings and symbolic representations of the human mind and its efficiency in texture analysis depends on the geometry of the scenes under study.

2.6.3 Model-based Methods

Model-based methods ([15] and [57]) interpret an image texture using fractal and stochastic models. The methods are based on the construction of a parametric image model that can be used to describe texture and synthesize it. The autoregressive model is an example of stochastic models that assumes a local interaction between image pixels in that pixel intensity value is a weighted sum of neighboring pixel intensities. The computational complexity of estimating the parameters is a major drawback of model-based methods.

2.6.4 Transform methods

Transform methods such as Fourier ([69] and [10]), Gabor [64], and Wavelet transforms [44] analyze the frequency content of the image. Fourier transform performs poorly in practice because it describes the global frequency content of an image without any reference to spatial localization. Gabor filters possess better localization properties in both the spatial and frequency domain but their usefulness is limited because spatial structures in textures can not be localized by a single filter resolution. Wavelet transforms provide multi-resolution analysis using a window function, whose width changes as the frequency changes. The wide range of wavelet functions enables one to choose wavelets best suited for texture analysis depending on the application. The drawback of a wavelet transform, however, is that it is not translation-invariant [43].

2.6.5 Statistical Methods

Statistical methods [31] represent texture using properties that govern the distributions and relationships between grey-level values of the image. Statistical

methods can be classified into first-order (one pixel), second-order (two pixels) and higher-order (three or more pixels) statistics based on the number of pixels defining the local feature. The first-order statistics (e.g. histograms) neglect the spatial interaction between image pixels and estimate properties like the average and variance of individual pixel values. On the other hand, second- (e.g. co-occurrence matrix) and higher-order statistics estimate properties of two or more pixel values occurring at specific locations relative to each other. The most commonly used methods are histograms, absolute gradient, run-length matrix, and co-occurrence matrix where,

- The **histogram** of an image provides a count of the total number of pixels that possess a given grey-level value.
- The gradient measures the spatial variation of grey-level values across the image and it can take positive or negative values depending on whether the grey level varies from dark to light or from light to dark. The **absolute gradient** ignores polarity since the presence of an abrupt or a smooth grey-level variation is what is of interest.
- The **Run-length matrix** capture the coarseness of texture by searching the image for runs of pixels having the same grey-level value, across a certain direction.
- The **Co-occurrence matrix** analyzes the grey level distribution of pairs of pixels and is also called the second order histogram. Contrast (difference between gray-level values of different objects in the image) and entropy (a measure of the randomness or homogeneity of the pixel distribution with respect to length or orientation) can be computed from co-occurrence matrix.

Studies showed that second-order statistical methods achieve higher discrimination rates than transform-based and structural methods [82]. Co-occurrence features are the most popular widely used second-order statistical features and it was shown that they outperform wavelet packets when applied to texture classification [80].

2.6.6 Texture analysis in medical imaging

Texture analysis methods are undergoing great development and utilization in medical imaging applications. During the past decade, researchers have shown the ability of texture analysis methods to extract information from medical images, obtained with different imaging modalities, that is not easily extracted by visual inspection [4], [19] [22], [23], [35],[43], [46], [60], [64], [65], [79] and [85]. For example, in segmenting anatomical structures based on their texture characteristics, alterations in the tissue of associated anatomical structures may occur. Normally, such alterations can be detected by histological examination but sometimes not by visual inspection of the tissue's image, whereas they may be demonstrated by statistically analyzing the pixel distribution of the structure's image.

Most medical applications use texture to classify regions of interest in images, to segment different anatomical structures [5], [19], [65], [79] and [85], or to differentiate between healthy and pathological tissue [4], [22], [23], [35],[43], [46], [60] and [64]. The procedure generally is to compute a large set of texture parameters, and then determine which of them provides the required discrimination. Such analysis remains limited by the restricted resolution of medical images, which makes it a promising method based on improvements in the quality of medical images.

2.7 Medical image segmentation

Many medical imaging applications inevitably use image segmentation to automate or facilitate the delineation of anatomical structures and other regions of interest. Image segmentation is the partitioning of an image into non-overlapping, constituent regions that are homogeneous with respect to some characteristic such as intensity or texture [31], [54]. Many segmentation techniques have been reported in literature, however there is no single method that yields acceptable results for all medical images, nor are all methods equally good for a particular type of image. Nevertheless, methods that are specialized to particular applications can often achieve better performance by taking prior knowledge into account. In this section, we describe common approaches that have appeared in literature on medical image segmentation and discuss their advantages and disadvantages. The reader can refer to

[21] for a detailed survey. Although each technique is described separately, multiple techniques are often combined to solve different segmentation problems.

2.7.1 Thresholding

Image thresholding [70] is the simplest segmentation process that divides an image into two segments only. A thresholding procedure attempts to determine an intensity value, called the threshold, where segmentation is achieved by grouping all pixels with intensity greater than the threshold into one segment and all other pixels into another segment. Determination of more than one threshold value is called multithresholding, and is used when there are variations in intensity levels of an image. Thresholding becomes a simple effective segmentation technique when different image structures have contrasting intensities or other quantifiable features. However, normally this condition is hard to meet in medical images, thus making threshold(s) selection a non-trivial job. The major drawbacks of thresholding are that in its simplest form only two classes are generated, and it does not take into account the spatial characteristics of an image. Accordingly, thresholding is sensitive to noise and intensity inhomogeneities which can normally occur in medical images.

2.7.2 Region-growing

Region growing [32] is a bottom-up technique that starts with a set of pixels known as seed pixels. Regions are grown from these seeds by adding neighbouring pixels that satisfy homogeneity criteria, thus increasing the size of each region (Fig 11). When the growth of one region stops another seed pixel is chosen which does not yet belong to any region and region growing starts again. The pixels that are considered are determined by whether 4- or 8-connectivity is being used. Region growing only works well if the initial seeds are properly representative of the regions of interest.

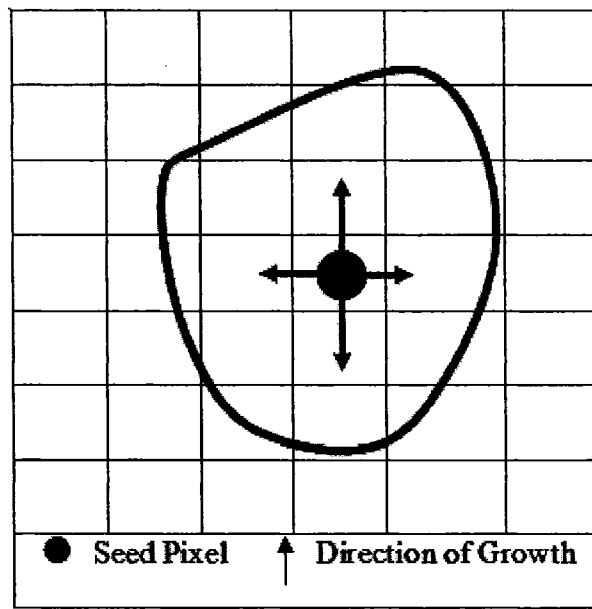


Fig 11. Illustration of region growing

The primary disadvantage of region growing is that it requires manual interaction to obtain a seed point for every region to be extracted. Besides, starting with a particular seed to grow a particular region completely before trying other seeds biases the segmentation in favour of the regions which are segmented first. This means that different choices of seeds may give different segmentation results. Another disadvantage is that ambiguities around edges of adjacent regions may not be resolved correctly. Region growing can also be sensitive to noise, causing extracted regions to have holes or even become disconnected.

Region growing is not often used solely in medical image segmentation, but within a set of image processing operations particularly for the delineation of small, simple structures such as tumors and lesions [27][61].

2.7.3 Artificial Neural Networks (ANNs)

ANNs are massively parallel networks of processing elements “neurodes” that attempt to model the basic architecture of the human brain, particularly its ability to parallel process information. Neurodes are analogous to physical neurons and they serve as the loci for mathematical operation. They are connected by mathematical weights (analogous to physical axons) that either emphasize or de-emphasize particular connections between them. Fig 12 shows the structure of a typical “back-propagation” ANN, one of the most often used network in many applications.

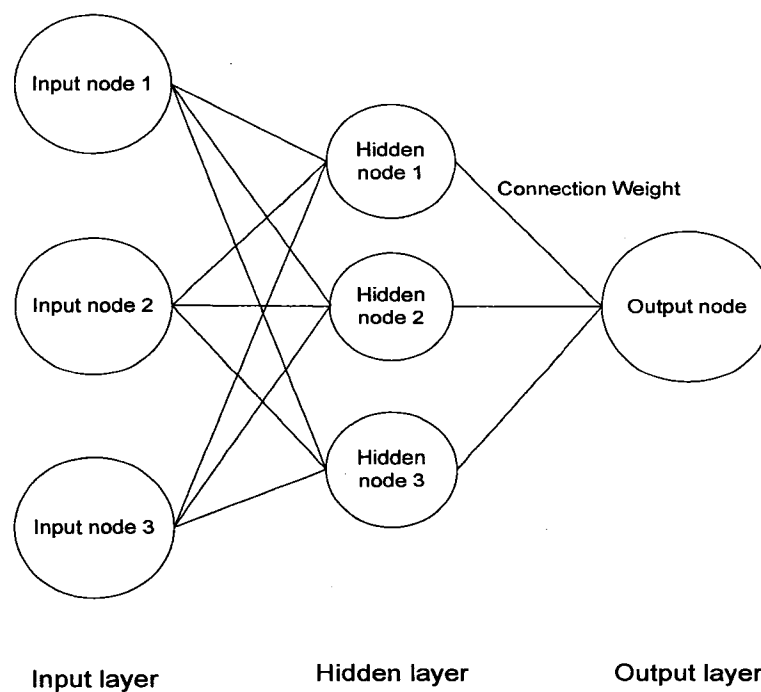


Fig 12. The structure of a typical back-propagation ANN.

The application of neural networks for image segmentation can be performed in a variety of ways. The widest use in medical imaging is as a classifier [26], as a

clustering method [67], or for deformable models [52]. Because of the many interconnections used in ANNs, spatial information can be integrated into their classification procedures.

Using ANNs in image segmentation does not require any well described and explicit properties or relationship of objects to be recognized, the network learn the general features from a set of training patterns. The major drawback of ANNs is that designing the network is mainly a trial and error as the effects of varying the number of units in each layer are poorly understood. Besides, the preparation of the training patterns is time consuming, as large sets have to be used for effective network training. Although ANNs are inherently parallel, they are usually simulated on standard serial computers thus reducing their potential computational advantage.

2.7.4 Deformable models

Segmenting structures to a compact geometric representation is difficult in medical images due to the sheer size of the datasets, the complexity, and the variability of the anatomic shapes of interest. Moreover, sampling artifacts, spatial aliasing, and noise may cause the boundaries of structures to be indistinct and disconnected. Extracting boundary elements that belong to the same structure and integrating them into a coherent and uniform model is a challenge. Traditional low-level image processing techniques, such as region growing, edge detection, and mathematical morphology operations, consider only local image information which results in incorrect assumptions during the integration process and thus generate infeasible object boundaries. As a result, these model-free techniques usually require considerable amounts of expert interactive guidance. Deformable models are a promising model-based approach to computer-assisted medical image analysis. The ability of deformable models to segment, match, and track images of anatomic structures is the reason behind their widely recognized potency. Deformable models exploit (bottom-up) constraints derived from the image data together with (top-down) *a priori* knowledge about the location, size, and shape of anatomic structures. Employing geometric representations such as splines, which involve many degrees of freedom, deformable model geometry usually permits broad shape coverage. The

degrees of freedom are governed by physical principles, which intuitively provide meaningful behavior, and are not permitted to evolve independently. The name “deformable models” has originated from the use of elasticity theory at the physical level, generally within a Lagrangian dynamics setting [48]. Through a computational physics simulation, the model responds dynamically to applied simulated forces in a natural and predictable way. The equilibrium state of the dynamic model is characterized by a minimum of the potential energy of the model subject to imposed constraints which deform the model such that it fits the data.

The deformable model that has attracted the most attention to date is popularly known as “snakes.” Active contour models known as snakes or energy minimizing curves were introduced by Kass et al. [36] for boundary segmentation in images. They usually consist of an initial model (contour) which is deformed until reaching a final location guided by external and internal forces. The external forces are derived from the gradient of the image under consideration leading the snake toward its salient characteristics. Internal forces are derived from the active contour itself and control its deformation. The snake will evolve towards a minimum of a global energy function which includes its forces.

Mathematically, a deformable model moves according to its dynamic equations and seeks the minimum of a given energy function [36]. The deformation of a typical 2-D deformable model can be characterized by the following dynamic equation [21]:

$$\mu(s)\frac{\partial^2 x(s,t)}{\partial t^2} + \gamma(s)\frac{\partial x(s,t)}{\partial t} = F_{\text{int}} + F_{\text{ext}} \quad (1)$$

Where $x(s,t) = (x(s,t), y(s,t))$ is the position of the model at a given time t , and $\mu(s)$, $\gamma(s)$ represent the mass density and damping density of the model, respectively. Eq. (1) causes the model to move according to the direction and magnitude of the forces on the right hand side. The most commonly used internal forces are

$$F_{\text{int}} = \frac{\partial}{\partial s} \left(\alpha(s) \frac{\partial x(s,t)}{\partial s} \right) - \frac{\partial^2}{\partial s^2} \left(\beta(s) \frac{\partial^2 x}{\partial s^2} \right) \quad (2)$$

which represent internal stretching and bending forces. The most commonly used external forces are computed as the gradient of an edge map.

Snakes have become quite popular for a variety of applications in medical imaging. Among the first and primary uses of deformable models in medical image analysis was to segment structures in 2D images. For example, snakes have been employed for the segmentation of myocardial heart boundaries as a prerequisite from which such vital information such as ejection-fraction ratio, heart output, and ventricular volume ratio can be computed [28] and [66]. Davatzikos and Prince used active contour models to map outer cortex in brain images [18]. Typically a deformable model is initialized near the object of interest and allowed to deform until it reaches the targeted object, where users can manually fine tune the model. Once the user is satisfied with the result on an initial image slice, the fitted contour model may then be used as the initial boundary approximation for neighboring slices. These models are then deformed and propagated until all slices have been processed. The resulting sequence of 2D contours can then be connected to form a continuous 3D surface model [48]. Image segmentation based on deformable models has been shown to be efficient in the segmentation of anatomical structures mainly due to its ability to exploit the image data as well as the prior approximate knowledge about the location, shape and dimension of structures. The interested reader can refer to [48] for an exhaustive review of the application of deformable methods to medical images.

The main advantages of deformable models are their ability to directly generate closed parametric curves or surfaces from images and their incorporation of a smoothness constraint that provides robustness to noise and spurious edges [21]. On the other hand, deformable models suffer from many drawbacks. Firstly, they require manual interaction to place an initial model and choose appropriate parameters [21]. The snake initialization accuracy influences significantly the segmentation, as disturbing image gradients which do not belong to the actual object contour can attract the snake into local energy minima. Secondly, deformable models can exhibit poor convergence to concave boundaries [21]. However, this difficulty can be alleviated somewhat through the use of pressure forces [14] and other modified external force models. Thirdly, the deformable models ability to automatically handle

topology changes turns out to be a liability in applications where the object to be segmented has a known topology that must be preserved [81]. Lastly, they require to a greater or lesser degree, a high computational effort, which renders them inappropriate for applications needing fast response [81].

2.7.5 Generalized Hough transform

Most of the usual segmentation algorithms rely on local image information, such as edges and gray levels, and may fail if the initialization is performed too far away from the expected solution. For example, snakes algorithm lacks foresight because the curve propagates according to a differential equation where the snakes' particles move under the influence of a small neighborhood of image pixels. If a full automatic object extraction is required, global information about the structure of interest (i.e. shape) has to be encoded in the segmentation algorithm.

The Generalized Hough transform (GHT) was proposed by Ballard [7] to detect shapes of no simple analytical form in which a look-up table is used to define the positions and orientations of boundary points with respect to a reference point. The edge direction at each pixel is measured and the corresponding position vector is retrieved from the lookup table. Then the cell that represents the reference position in the Hough domain is increased.

Fig 13 shows the relevant geometry and the table shows the form of the lookup table where (x_c, y_c) is reference point, (x, y) is an edge point, β is the edge point direction, ϕ is the edge point orientation and r is the distance between the edge point and the reference point.

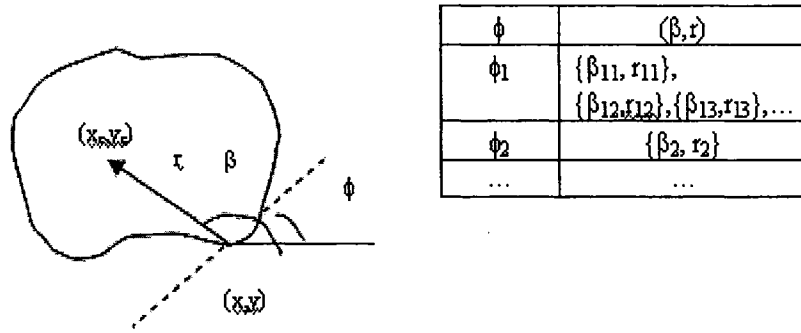


Fig 13. An illustration of GHT parameters and lookup table

Using Fig 13, the GHT algorithm can be summarized in the following steps [34]

- A- Examine the boundary points of a standard shape to construct the lookup table
 - 1- Choose a reference point x_c, y_c for the shape
 - 2- For each boundary point (x, y) , find ϕ , β , and find r where $r = (x_c, y_c) - (x, y)$
 - 3- Store r , β as a function of ϕ
 - 4- The lookup table is constructed where ϕ is its index and each ϕ may have many values of r , β
- B- Applying Hough transform to the image
 - 5- For each edge pixel (x, y) in the image
 - a. Find the entry in the lookup table that corresponds to its ϕ
 - b. Increment all corresponding points $a = (x, y) + r$ and store the result in accumulator A
 - 6- Find maxima in A
 - 7- Map each maxima back to image space

The Hough transform has been used to detect objects of regular shapes in medical images. For example, Solaiman et al [78] has applied the Hough transform to locate the aorta in ultrasound images. Fitton et al [25] used the Hough transform to automatically assess the regional systolic thickening of the left ventricle from cardiac wall segmentation, where they approximated the shape of the epicardial contour with a circle. The Hough transform was used to detect the circle parameters and then a number of control points were uniformly placed along the estimated circle boundary

for further boundary refinement. Because of the irregular shape of the prostate, the Hough transform can not be used in our research; we need a general algorithm that can deal with irregular shapes. Fortunately, the generalized Hough transform proved successful in detecting objects of irregular shapes [83], [20][63] and it is applicable to our problem. However, its main drawbacks are its substantial computational and storage requirements that become especially acute when object orientation and scale have to be considered.

CHAPTER III

RELATED WORK

3.1 Introduction

In this chapter, we provide an overview of current methods used for prostate boundary detection from ultrasonographic images. Ultrasound has been the main imaging modality for prostate related applications since it is inexpensive, easy to use, accessible, can be viewed in real time, and it has no adverse effect on patients. However, the methods discussed are by no means limited to ultrasonographic images, and can be applied in different image applications, taking into consideration the limitations of each imaging method. Detecting the prostate boundary plays a key role in many applications, such as the accurate placement of the needles in biopsy, the assignment of the appropriate therapy in cancer treatment, and the measurement of the prostate gland volume [77]. Since manual delineation of the boundaries is tedious and sensitive to observer bias and experience, automatic segmentation has a significant advantage over manual annotation. On the other hand, automatic segmentation of ultrasound images is a challenging task because:

- Ultrasound images have low intensity contrast between prostate and non prostate regions.
- Images contain a considerable amount of noise.
- The prostate contour in images is often incomplete.
- The prostate does not have one unique shape.

In this chapter, we focus on providing an introduction to the different algorithms that were proposed by other researchers to improve the efficiency of ultrasound prostate segmentation (or simply boundary detection) and the pros and cons of each method.

3.2 Two-dimensional Prostate Boundary Detection from Ultrasonographic Images

This section presents a review of major publications for 2D prostate boundary detection. Accordingly, the prostate image segmentation methods can be classified into three types: edge-based, texture-based, and model-based methods.

3.2.1 Edge-Based Detection Methods

In edge-based methods, the prostate boundary is outlined by using two subsequent steps. The first step is using edge detectors to identify all the edges in the image. Pixels are classified into edge and non-edge using image features such as local maxima of directional intensity gradients. The second subsequent step is an edge recognition process to select and link edge pixels to produce a continuous boundary of the prostate.

Aarnink et al [2] have developed a practical method based on minimum and maximum filtering using an approximation of a nonlinear Laplace filter to objectively detect the prostate contour in a series of consecutive cross-sections for prostate volume measurements in transrectal ultrasonographic images. Using this algorithm, the authors were able to obtain the second derivative and the gradient images that represent possible edges and the corresponding strength of those edges. The edges are enhanced, emphasized by relaxation, selected, linked and interpolated to form a closed prostate boundary. With the manually indicated prostate center as the starting point, specific features (light-to-dark transitions at edges) are extracted for edge enhancement and knowledge-based (such as the expected kidney-like shape) search strategies are applied for selecting the correct edges. They used a radial edge search strategy starting at the manually indicated prostate center for the upper prostate part and a linear search strategy for the lower part. The problem with this method is that artifacts such as cysts, calcification, and shadowing can lead to erroneous edges. The authors further improved the edge detection and localization, by introducing a multi-resolution edge detection scheme [3]. They used the local standard deviation to differentiate between the homogeneous regions and the areas that showed intensity transition. Areas with high possibility of edge appearance, as indicated by high standard deviation, were analyzed using smaller filter sizes to improve edge

localization. More interpolation to find a closed contour is therefore needed, and the definition of prior knowledge becomes more essential.

Liu et al [40] introduced a radial bas-relief (RBR) method, which was extended from a darkroom technique used in conventional photography, to segment the prostate boundary from ultrasound images. Multi-resolution filtering was used and the resulting image set was superimposed to obtain a binary-like image in which the prostate boundary was enhanced. However, the RBR method would fail to detect the desired boundary if the image center and the object boundary centroid were not close and had a big deviation.

Pathak et al [56] used an edge-based technique for outlining the prostate boundary. First, the contrast of the image was enhanced using a method called *sticks*. The resulting image was then smoothed by a filter, and then some prior knowledge of the prostate shape and its appearance in ultrasonic images was used to detect the most probable prostate edges. The detected edges were overlaid on top of the image and then presented as a visual guide to the observers for manually delineating the prostate boundary. An important issue in this study is that although the inter-observer consistency in prostate delineation was improved when the edge detection results were used to guide manual outlining, the manual interference is still a source of error and results should be better if the delineation process is automated.

Edge-based boundary detection methods are very straightforward methods that typically locate edges that correspond to local peaks in image intensity gradient. These methods can perform well if the boundary is clearly defined. However, because of the ultrasonographic images poor quality, the application of these methods leads to false boundaries in highly textured areas as well as missing boundaries in not well delineated prostate boundary areas.

3.2.2 Texture-Based Detection Methods

In texture-based methods, pixels are classified into target regions and non target regions using the texture information which can produce an edge map by creating a border between regions that have different textures. Richard and Keen [68] extracted the prostate boundary by segmenting 2D images of the prostate gland into prostate

and non-prostate regions. They used a pixel classifier based on four texture energy measures associated with each pixel in the image and a clustering procedure was used to associate each pixel with its most probable class. The authors, however, claimed that their algorithm is computational expensive and the number of classes produced by the clustering procedure is unpredictable. They acknowledged that the effect of using texture information is marginal and that better results can be obtained if their algorithm is combined with other edge-detection methods.

3.2.3 Model-Based Detection Methods

Studies have shown that model-based segmentation methods are efficient in delineating object boundaries [48]. These methods integrate some prior knowledge, such as shape information and imaging features, into the model to improve the boundary detection algorithms. This section reviews two different concepts that refer to model-based methods that have been applied to prostate boundary detection. The first concept is based on deformable contour models while the other one is based on statistical models.

3.2.3.1 Deformable Contour Models

Deformable contour models, introduced by Kass et al. [36] and known as active contour models or snakes, delineate object boundaries by using closed curves or surfaces that deform under the influence of internal and external forces. Deformable models have been extensively investigated in literature as an attractive tool for image segmentation and boundary detection.

Pathak et al. [55] presented an algorithm based on snakes to detect the prostate boundary from transrectal ultrasonographic images. They used the sticks algorithm [17] to enhance the contrast along the edges, followed by a snake model initialized with manually specified initial curve. To initiate the boundary detection, the user has to input an initial curve for each ultrasonographic image. The results acquired are found to be dependent on the position of the initial contour to the prostate boundaries. If the initial contour is reasonably close to the boundaries, the algorithm delineates the prostate boundaries successfully and vice versa.

Ladak et al. [39] developed a method in which the user selects four points located on the prostate boundary from which the initial contour is estimated by cubic interpolation functions and shape information. Gradient direction information was used to attract the contour to the prostate boundaries. If the algorithm failed to detect the correct boundary due to improper initial points (which is a major drawback), the detected boundary was manually edited and deformed again to obtain better results.

Attempting to address the problem of contour initialization, Knoll et al. [37] and [38] proposed an algorithm to represent particular prostate shapes and restrict the elastic deformation. In their algorithm, the authors applied localized multi-scale contour parameterization based on the 1D dyadic wavelet transform. The starting contour was initialized using a binary multi-scale pattern matching, which compares a training set of object models against the real image data. The internal curve deformation forces were implemented using multi-scale parametrical contour analysis. Their experiments had proved the robustness and efficiency of their algorithm compared to conventional snakes.

3.2.3.2 Statistical Models

In statistical models, the variations of parameters in a training set are coded and characterized in a compact manner. Estimated parameters are obtained from available segmented images and are used to segment new images. The result can be incorporated into the model thus updating a priori information available to the system.

Prater and Richard [62] presented a method for segmentation of the prostate in transrectal ultrasound images based on feed-forward neural networks where images are segmented into prostate and non-prostate regions. The authors proposed three neural network architectures which are trained using a small portion of a training image (segmented by an expert) and then applied to the entire training image. Although this method could provide a good result of segmentation, it requires extensive training and thus complicates the detection process. Moreover, it is difficult to incorporate user-specified boundary information into the neural networks.

Lorenz et al. [42] extracted the prostate boundaries using the Markov random field (MRF). They assumed the contour sequence to be a 2D first order Markov random process, and incorporated prior shape knowledge about the contour by clique potentials defined on a neighborhood system. The contour is estimated iteratively on the basis of the maximum a posteriori principle and the results were further improved by incorporating three-dimensional information on neighboring slices in a volume data set. The drawbacks of the MRF method are: the difficulty to properly select the parameters that control the strength of spatial interaction, and its intensive computational load.

Wu et al. [84] proposed a model-based boundary recognition method called feature-modeling to detect the prostate boundary automatically. In their algorithm, the authors modeled the boundaries using conventional point distribution estimation method where some specific information about the prostate (such as the shape, actual size, relative position to the ultrasonic probe, and boundary orientation) is integrated. Subsequently, they used a genetic algorithm to perform a robust search of the object boundary with model constraints. Although the authors claimed that their algorithm has achieved good accuracy and robustness, the specifications of their model requires that the central point of the ultrasonic probe must be visible in the image; however it is not captured in most ultrasound examinations.

Shen *et al.* [77] introduced a statistical shape model to automatically segment the prostate in transrectal ultrasound images. The model consisted of three parts: the calculation of the statistical shape from the prostate sample, the hierarchical representation of the image features using the Gabor filter bank, and the hierarchical deformable segmentation. The shape statistics was calculated from a set of training samples that are manually outlined from the ultrasound images. The image features are hierarchically represented by a set of rotation-invariant features reconstructed from the Gabor filter bank. These features were used as the image attributes for driving the prostate shape model to its correct position in the ultrasound image. The average shape model was rigidly transformed to a position that optimally matches the rotation invariant image features, to determine the model initialization. The model is then hierarchically deformed under the forces from the features, the internal and

statistical constraints. The experimental results were promising and were close to annotations provided by human experts.

Gong et al. [24] incorporated prior knowledge of prostate shapes in a deformation-based method, to automatically segment prostate in ultrasound images. The prostate shapes were modeled using deformable super-ellipses. The results were compared with manual outlining from several human experts and shown to be promising.

Chiu et al. [13] introduced a semi-automatic segmentation algorithm based on the dyadic wavelet transform (DWT) and the discrete dynamic contour (DDC). A spline interpolation method was used to determine the initial contour based on four user-defined initial points. The DDC model then refined the initial contour based on the approximate coefficients and the wavelet coefficients generated using the DWT. The DDC model was executed under two settings and a selection rule was used to choose the best contour based on the contours produced. The authors compared the final contour produced by the proposed algorithm with the manual contour outlined by an expert observer and claimed that the average difference between them is less than 3 pixels.

Betrouni *et al.* [9] discussed a method for the automatic segmentation of trans-abdominal ultrasound images of the prostate. In this method, a filter is applied to enhance the contours without modifying the image information. This filter combines adaptive morphological filtering and median filtering to detect the noise-containing regions and smooth these areas. Then a heuristic optimization algorithm searches for the contour initialized from a prostate model. The authors compared the resulting contours with those obtained by manual segmentation and claimed that the average distance between the contours was 2.5 mm.

3.3 Discussion

Recent studies are focused more on statistical model based algorithms than deformable models. Deformable models based methods use only local constraints such as gradients and shape smoothness, therefore the results heavily depend on individual images. Statistical-model-based segmentation methods, on the other hand,

characterize and use all possible variations in the training set to identify a valid instance. Information obtained in the training process can serve as constraints or prior knowledge for the segmentation process, thereby achieving a trade-off between the prior knowledge (obtained during training) and the local information in the processed image [86].

By analyzing the existing literature, the error resulting from applying prostate segmentation methods may increase considerably when the image contains shadows with similar gray level and texture attached to the prostate, and/or when boundary segments are missing. Another obstacle that faces segmentation is the lack of sufficient number of training (gold) samples if a learning technique is used. Although algorithms based on active contours have been used successfully, their major drawback is that they depend on user interaction to determine the initial contour.

Therefore, a new segmentation approach should ideally possess certain properties:

- User interaction (e.g. defining seed points or manually placing initial contour) should be eliminated due to its drawbacks such as time consumption, human bias and/or error.
- Sample-based learning should be avoided because it is difficult to provide a large number of training samples in medical environments.
- Robustness of the segmentation algorithm with respect to the presence of noise and shadow is crucial.
- Shape information should be incorporated into segmentation algorithms to be able to estimate contour segments that are missing in some areas.

In this dissertation, we establish a straightforward algorithm which attempts to avoid the problems that exist in literature and to satisfy the above conditions as much as possible.

CHAPTER IV

ESTIMATION OF THE PROSTATE CAPSULE USING SHAPE INFORMATION

4.1 Introduction

In order to automatically identify the capsule of the prostate and replace the arduous and costly manual process of detecting it, a software algorithm was developed that recognizes the capsule utilizing elements of prostate anatomy and shape. Certain anatomical features make capsule generally detectable; however, the capsule is unrecognizable in some areas because of the naturally occurring intrusion of muscle into the prostate gland at the anterior apex and fusion of extraprostatic connective tissue with the prostate gland at its base. At these regions where the prostate capsule disappears, its contours need to be reproduced by drawing a continuing contour line from those areas where the capsule can be objectively recognized, also taking into account the natural shape of the prostate gland.

In this chapter, we first highlight the research efforts in the literature that classified cells in histopathologic images and can be applied to our problem. We then introduce a mathematical model that provides a standard prostate shape to be used in conjunction with Generalized Hough Transform (GHT) to detect the prostate capsule as well as approximate the missing parts of the capsule where it disappears to a standard shape. We also present another algorithm based on least squares curve fitting technique that uses the prostate shape equation to merge the previously detected capsule parts with the curve equation to produce an approximated smoothed curve that represents the prostate capsule.

4.2 Detecting Histological Patterns of Elastic Fibers within the Prostate Capsule

As we have previously pointed out in chapter 2, the elastic fibers within the prostate capsule can be clearly recognized under the microscope and also under high resolution of scanned digital images. In order to correctly locate those lines, it is essential to detect the parenchymal outer contour of the prostatic glandular epithelial

elements (Fig 14), since the capsule is normally located between this contour and the perimeter of the slice.



Fig 14. A prostate slice with parenchymal contour (inner line), slice perimeter (outer line), and the prostate capsule (dashed line).

Classification of cells in histopathologic images is an important problem in many clinical and research activities. Traditional histopathologic techniques remain labor-intensive and inherently subjective based on the personal judgment of pathologists. The development of automated pathology has remained out of reach essentially due to the complexity of imagery. Nowadays, with developments in machine vision, image processing systems, and computer hardware, pathologists' methodologies could be complemented by providing an automated and objective approach to analyze histopathologic images. Analyzing cell images can be considered as an image segmentation problem where cells or their kernels should be extracted [53].

There are several attempts in literature to classify tissues of histopathologic images using texture analysis and image morphology [19], [29], [30], [53] and [58].

Nedzved et al. [53] proposed two segmentation algorithms for histology cell images by means of gray-scale thinning, mathematical morphology and split/merge

operations. Their algorithm produced good results for most of the images; however the segmentation result depends on the quality of preparation and on the coloring of histology images.

Diamond et al [19] used prostate slices cut from whole-mount radical prostatectomy to identify tissue abnormalities in prostate histology. The images of the slices are captured at x40 objective magnification using a microscope and a digital camera and overlapped by 10% for registration purposes. Since texture analysis is based on the interrelationship between pixel intensities, the authors chose a subimage size of 100x100 to define a high degree of detail, for processing at a time. They used texture and morphological characteristics of the scenes in the subimages to classify the different tissue types. By investigating Haralick texture features, they found that Haralick 4 (H4) is more appropriate to distinguish between stroma and prostatic adenocarcinomas while the analysis of morphological characteristics allowed the identification of normal tissues. Normal tissue exhibits larger areas of associated lumen, thus the identification of lumen objects using mathematical morphology defines the epithelial layer. The authors were able to correctly classify 79.3% of subregions of small scenes. Their methodology also succeeded in classifying the different tissues when applied to whole slide images via scanning technology.

Petushi et al. [58] developed an automated method to detect and identify microscopic structures on histology slides. They were able to identify fat cells, stroma, nuclei of cells of epithelial origin, and other two types of nuclei that represent inflammatory cells and cancer cells. The slides were scanned using a 40X magnification lens, covering almost all the tissue. Each slide image is composed of 400 sub-images each is 460x620 pixels. The algorithm starts by an off-line learning phase to extract intensity mean, intensity STD, and shape area for each type of nuclei, while for the stroma and fat like structures only the intensity mean and STD features are extracted. To segment the regions of interest that represent the three types of cell nuclei, the authors used optimal adaptive thresholding (based on histogram partitioning to automatically determine the optimal thresholds) with local morphological opening and closing operations. The output from the segmentation step was then clustered and a binary decision tree was used as a classification method.

The authors were able to correctly identify the different tissue structures in H&E stained histology slides with $89\% \pm 0.8$ accuracy.

Based on the previous research efforts, we conclude that the collagenous fibers within the prostate capsule as well as the epithelial cells can be automatically identified using either of the techniques mentioned in [19] and [58], given that the slides are scanned at 40X magnification. By detecting the epithelial cells, the parenchymal contour can therefore be generated. As for the tissue parts where the prostate capsule exists, the algorithms mentioned above can automatically detect them and mark them on the slices' images to be used as inputs to our algorithms which we will explain in the following sections.

4.3 A Mathematical model for a standard prostate shape top down anterior to posterior

In general, any prostate has a standard shape as the one shown in Fig 15 where it has different parameters. This shape can be defined in terms of equations for each quadrant (four equations total) as follows [34]

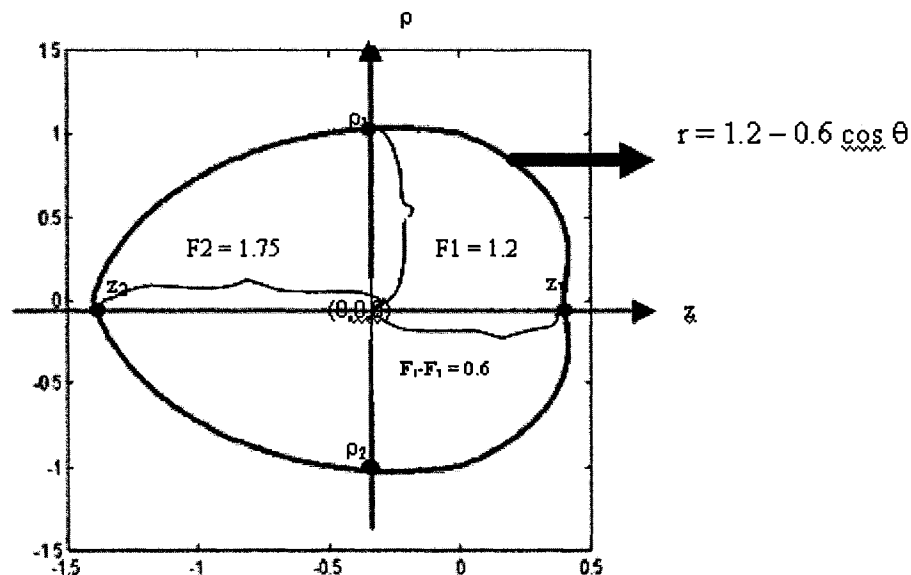


Fig 15. A standard prostate shape.

In the first quadrant, the curve's equation can be defined in terms of two equations

$$\begin{aligned} z &= (F1 - F3 \cos \theta) \cos \theta \\ \rho &= (F1 - F3 \cos \theta) \sin \theta \end{aligned}$$

Where $0 \leq \theta \leq \pi/2$

For the second quadrant where $\pi/2 \leq \theta \leq \pi$

$$\begin{aligned} z &= \left(\frac{2}{\Pi} (F2 - F1)\theta + 2F1 - F2 \right) \cos \theta \\ \rho &= \left(\frac{2}{\Pi} (F2 - F1)\theta + 2F1 - F2 \right) \sin \theta \end{aligned}$$

Similarly, the third and fourth quadrants curves can be defined by considering the shape's symmetry.

The anterior/posterior ratio will be defined as R where R is equal

$$R = \frac{Z1}{-Z2} = \frac{F1 - F3}{F2}$$

Where

$$F1 = \rho_{\max}$$

$$F2 = \frac{\Delta z_{\max}}{1 + R}$$

$$F3 = \rho_{\max} - \left(\frac{R}{1 + R} \right) \Delta z_{\max}$$

And

$$\begin{aligned} \rho_{\max} &= F1 \\ \Delta z_{\max} &= F1 - F3 + F2 = \rho_{\max} - F3 + F2 \end{aligned}$$

Up to this point, a standard shape of a complete prostate gland was considered. We now need to find a standard equation that defines a prostate slice. A prostate slice can be viewed as shown in Fig 16 where a standard equation can be defined as follows

$$\left(\frac{x}{F} \right)^2 3.32552 + \left(\frac{y}{F} 1.8142857 - 0.27 \right)^2 = 1 \quad \text{----- (3)}$$

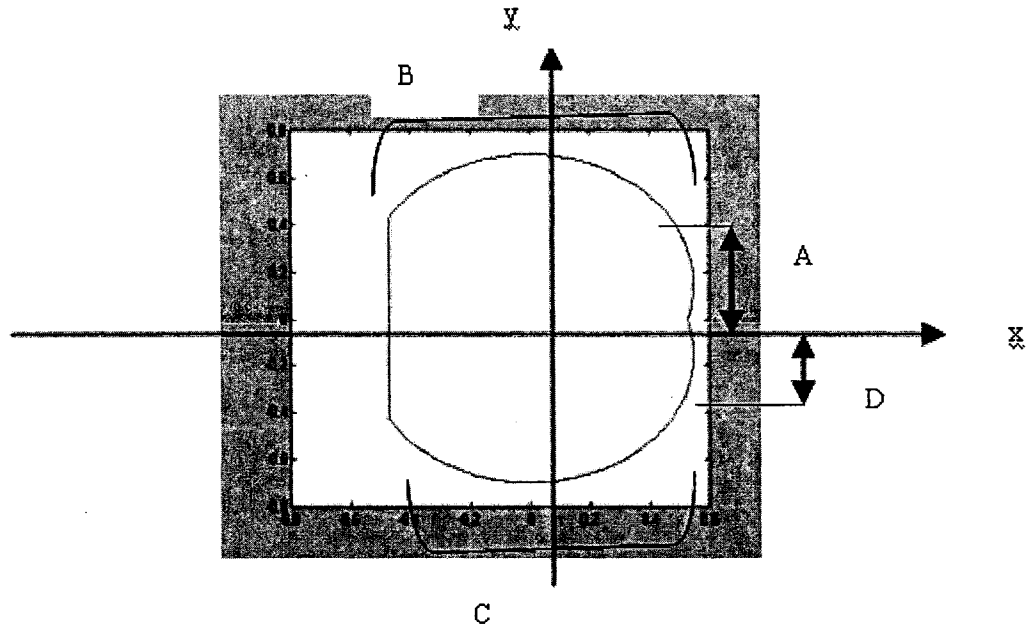


Fig 16. A standard shape of a prostate slice.

Notice that Fig 16 consists of four curves marked as A, B, C and D where each of these curves represents a case of equation 3 with different parameters values.

For curve A equation, substitute in equation 3 with y from 0 to 0.1488188F, and find

x

$$\text{Therefore } x = F \times \sqrt{\frac{1 - \left(\frac{1.8142857}{F} y - 0.27 \right)^2}{3.32552}} \quad \text{----- (4)}$$

For curve B, substitute with $y = [0.1488188 + 0.55118 \sin \theta] F$ for x;

Where $0 < \theta < 0.83\pi$

$$x = \pm F \times \sqrt{\frac{1 - \left(\frac{1.8142857}{F} y - 0.27 \right)^2}{3.32552}} \quad + \text{ for } 0 < \theta < \pi/2, \quad - \text{ for } \pi/2 < \theta < 0.83\pi \quad \text{----- (5)}$$

$\pi/2 < \theta < 0.83\pi$ ----- (5)

For curve C, substitute with $y = [0.1488188 - 0.55118 \sin\theta] F$ for x ;

Where $0.17 < \theta < \pi$

$$x = -F \times \sqrt{\frac{1 - \left(\frac{1.8142857}{F} y - 0.27 \right)^2}{3.32552}} \quad - \text{ for } 0.17\pi < \theta < \pi/2, \quad + \text{ for } \pi/2 < \theta < \pi \quad \text{----- (6)}$$

$\pi/2 < \theta < \pi$ ----- (6)

For curve D, substitute with $y = -0.1488188 F$ to 0 for x ;

$$x = F \times \sqrt{\frac{1 - \left(\frac{1.8142857}{F} y + 0.27 \right)^2}{3.32552}} \quad \text{----- (7)}$$

The above equations can be approximated by the Limaçon curve equation

$$r = b + a \cos \theta \quad \text{----- (8)}$$

Different shapes of the curve can be generated by varying the ratio of a to b as shown in Fig 17.

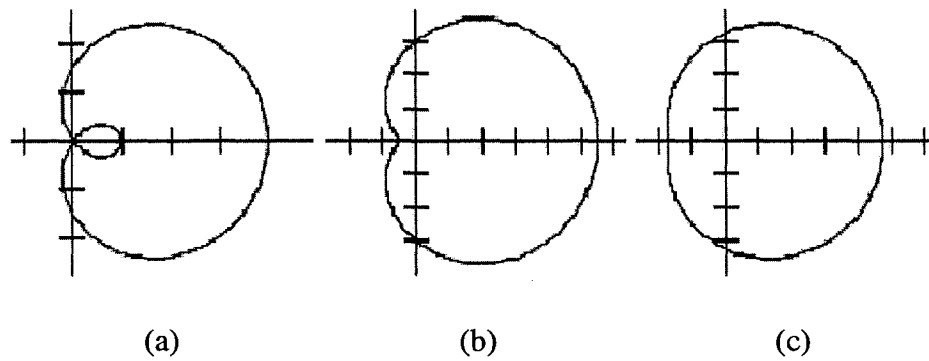


Fig 17. Limacon curves (a) when $a < b$, (b) when $a < b < 2a$, and (c) when $2a \leq b$.

The limaçon serves only as an approximation since there is always a degree of roundness to this shape. Therefore, the limaçon serves as a better shape than a circle but may not be as good as an ellipse where more elongated prostate shapes are observed.

4.4 Approach

We present a general process that utilizes two different shape algorithms to detect the prostate capsule. This process can be summarized as follows:

1. Using digital images of prostate slices scanned with 40x magnification, identify the input sections of the prostate capsule (the outer perimeter, the parenchymal contour, and the observable portions of the capsule) automatically using texture analysis techniques [19].
2. Call a shape algorithm to generate a curve that interpolates between the parts generated in step 1.
3. Adjust the generated curve so that it does not violate any constraints. In our case the constraint is that the curve should be between the parenchymal contour and the prostate perimeter.
4. Repeat steps 2 and 3 until a satisfactory threshold is acquired.

To achieve step 2, we have used two different shape algorithms: the Generalized Hough Transform (GHT) and the least squares shape algorithms. In the following sections we present them in details.

4.4.1 Generalized Hough Transform (GHT) shape algorithm

In chapter two, we have introduced the GHT algorithm and its mechanism, GHT can be applied to detect the prostate boundary by the use of prostate slice equations, defined in the mathematical model that was introduced in the previous section, as follows:

For a prostate slice

1. Choose a reference point x_c, y_c for the shape (It can be the central point)
2. For each boundary point $y = (x_i, y_i)$, find r where $r = (x_c, y_c) - (x_i, y_i)$ then substitute with y in equations 2,3,4, or 5 (according to the current quadrant) to get the corresponding curve equation x
3. Store r , y , and x in a lookup table (Table 1)
4. For each r in the lookup table, count the number of points that construct each curve occurrence and represent the counter by c
5. Choose the largest c for each r ; this represents the strongest curve occurrence.

Table 1: A lookup table for the proposed GHT.

r	(x, y)
r_1	$\{x_{11}, y_{11}\},$ $\{x_{12}, y_{12}\}, \{x_{13}, y_{13}\}, \dots$
r_2	$\{x_2, y_2\}$
\dots	\dots

Determining the boundary points in step 2 of the previous algorithm can be done by recognizing the histological pattern of the elastic and collagenous fibers within the prostate capsule as we have previously mentioned in section 1 of this chapter. In our experiments, we have used circle, limacon, and ellipse shapes as our equations for the GHT algorithm.

4.4.1.1 Implementing the GHT using the limacon shape equation

In implementing the GHT algorithm using the limacon equation, we have taken rotation into consideration thus adding another term to the limacon equation to become $r = b + a \cos(\theta + \Phi)$

A range of values is chosen for $a, b, \Phi, (x_c, y_c)$ where x_c, y_c is a reference point

For each boundary point (x, y) [boundary points represent the capsule parts]

For each x_c, y_c (the range covers the whole image)

For each a, b

Calculate $\theta = \tan^{-1}((y - y_c) / (x - x_c))$

Calculate $r = b + a \cos(\theta + \Phi)$ [Φ is configurable]

Calculate $r' = \sqrt{(x - x_c)^2 + (y - y_c)^2}$

If $r = r'$ (within certain threshold),

increase accumulator [The accumulator is a 5D array in a, b, x_c, y_c, Φ]

End for

End for

End for

We have set a threshold at which we consider the curve passing by a particular point if the point is within n pixels distance from that curve. The number of pixels n is calculated by $n = (d_1/d_2) * t$

Where d_1 is the diagonal of the image in pixels,

d_2 is the diagonal of the picture box of the GUI,

and t is a threshold that we set to 5

The accumulator is scanned to find the cell with the maximum count

The corresponding cell parameters (a, b, x_c, y_c, Φ) represent the resulted curve

In case that more than one curve is retrieved, the curve that has the minimum square error with respect to the optimal capsule line (drawn by the pathologist) is chosen

4.4.2 The least squares shape algorithm

The least squares method is a very popular technique used to compute estimations of parameters and to find the best fitting model for discrete data. It is widely used in literature to fit a function (which may represent a certain shape) to a set of data which can be used in many applications including medical imaging [59].

Assuming that we have a number n of discrete data $(x_1, y_1), (x_2, y_2), \dots, (x_n, y_n)$ and $f(x)$ is a function for fitting a curve. Therefore, $f(x)$ has the deviation (error) d from each data point, i.e. $d_1 = y_1 - f(x_1), d_2 = y_2 - f(x_2), \dots, d_n = y_n - f(x_n)$

The best-fit curve is the curve that has the minimal sum of the deviations squared from a given set of data [16], i.e. it is the curve that satisfies the following equation

$$\begin{aligned} \text{Minimum Least square error } (\Pi) &= d_1^2 + d_2^2 + \dots + d_{n-1}^2 + d_n^2 \\ &= \sum_{i=1}^n d_i^2 \\ &= \sum_{i=1}^n [y_i - f(x_i)]^2 \end{aligned}$$

4.4.2.1 Implementing the least squares using the limaçon shape equation

Using the limaçon equation, taking the rotation factor into consideration, the least squares algorithm can be summarized as follows:


```

Select range of values for the center of the curve (cx,cy)
Select range of values for the curve parameters (a, b)
Select range of values for the curve rotation angle (theta)
minError = infinity
FOR all values of a
  FOR all values of b
    FOR all values of cx
      FOR all values of cy
        FOR all values of theta
          Generate the curve points
          Compute the error in curve
          IF error < minError
            minError = error
            store curve parameters
          END IF
        END FOR
      END FOR
    END FOR
  END FOR
END FOR
Return the stored curve parameters

```

We have used the least square method to find the closest location of the prostate shape equation with respect to the parts of the capsule that are present in the tissue (Fig 18)

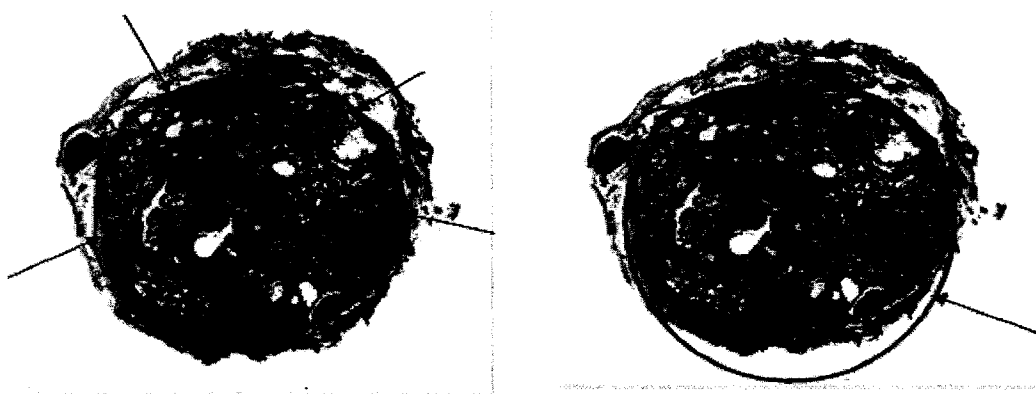


Fig 18. Least squares method and prostate shape equation. (a) Arrows point to the detected parts of the prostate capsule, (b) Arrow points to the curve representing the prostate shape located as close as possible to the capsule parts.

4.4.2.1.1 Known capsule regions preservation

Once the curve is positioned close to the capsule parts, parts of the shape curve is replaced by the capsule segments and a new curve is generated by connecting all the curve points and capsule points using cubic splines (Fig 19)



Fig 19. New shape curve after merging the capsule parts into the original shape curve.

This can be summarized as follows

```

FOR each segment on the boundary curve
    point1 = Closest point on the generated curve the first point on the segment
    point2 = Closest point on the generated curve the last point on the segment
    IF length of curve from point1 to point2 < ( total length of curve ) / 2
        remove curve points in the range from point1 to point2
    ELSE
        remove curve points in the range from point2 to point1
    END IF
    insert segment points into the curve
    smooth curve at connection points
END FOR

```

At the connection points, we used a smoothing technique which can be summarized as follows:

```

pivot = connection point
alpha = initial smoothing factor (between 0 and 1)
WHILE (alpha > threshold)
    p = get the next neighboring point
    compute the equation of the line connecting pivot to p
    d = length of the line
    replace p with the point at distance (1-alpha)*d from the pivot (on the line)
END WHILE

```

4.4.3 Curve Adjustment Algorithm

Sometimes the generated curve violates the constraint that states that the prostate capsule is typically located between the parenchymal contour and the prostate perimeter as shown in Fig 20.

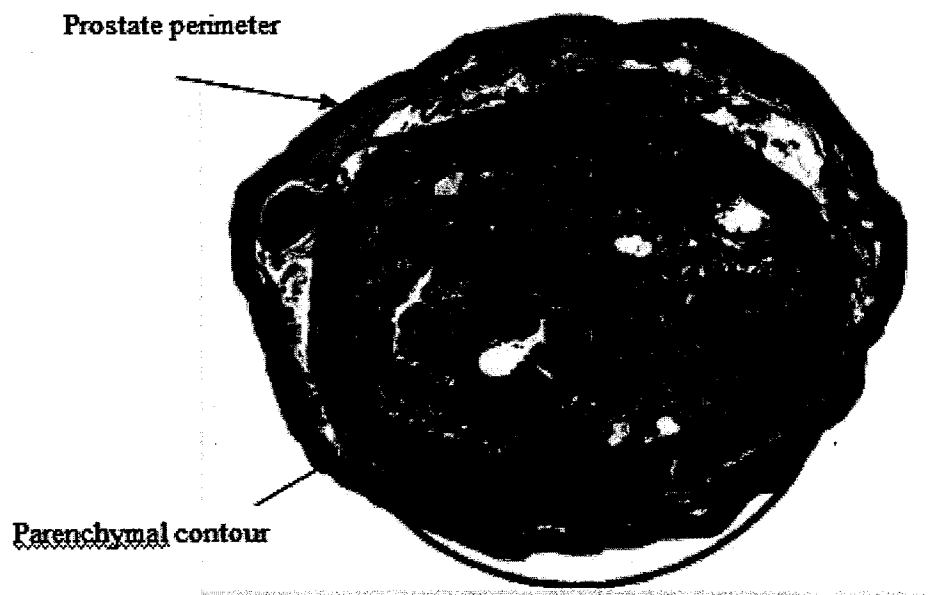


Fig 20. Shape curve extending beyond the prostate perimeter.

In this case, we use the flood fill algorithm [33] to relocate the curve parts that violates the constraint such that new points are generated between the 2 contours (Fig 21) for the least square algorithm to be executed again for better results.

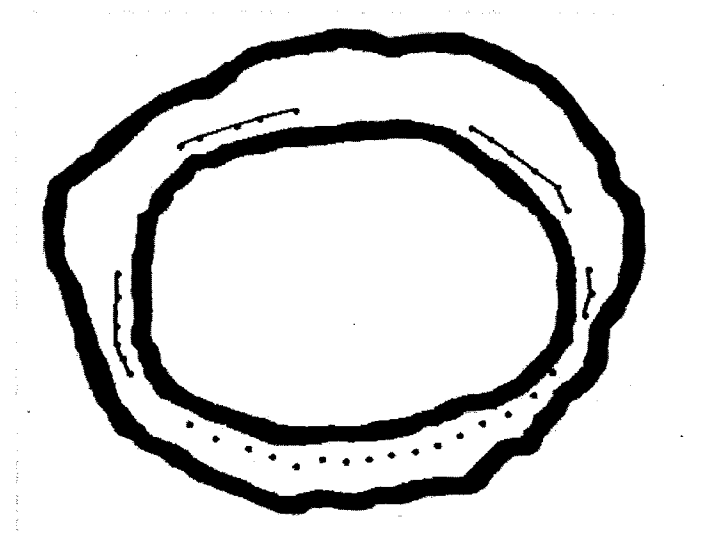


Fig 21. Contours.

4.5 Summary

In this chapter we presented two novel shape algorithms to detect the prostate capsule boundary with the use of Generalized Hough Transform (GHT) and least squares fitting along with prostate shape equations. The curve adjustment algorithm was used primarily to generate new boundary points to feed the shape algorithm for consecutive runs for improved shape fitting. However, in case one wishes to stop after a certain number of runs and the output curve extends beyond the slice perimeter or inside the parenchymal contour, the algorithm is used as a final step to enforce this constraint. This enforcement may result in some sharp edges; a curve smoothing technique can be added as a future extension to our algorithm to solve this problem.

CHAPTER V

IMPLEMENTATION AND EXPERIMENTAL RESULTS

5.1 Images preprocessing

The specimens used in our study are sliced every 5mm from apex to base, along the urethra and each slice is saved in a jpg file with a size of approximately 3000x2000 pixels. To speed up the algorithms processing time, we have reduced the size of each slice image by 50%. Our algorithms start with the assumption that the parenchymal contour and the prostate perimeter contour have been automatically predetermined by a texture based segmentation technique as we explained in chapter 4. Therefore, we have substituted this phase by manually outlining the two contours using adobe photoshop 7.0. We have chosen a distinct color for each contour that uniquely identifies it from the other colors in the slice. The RGB combination for the parenchymal and perimeter contours are chosen to be (60, 120, 60) and (120, 120, 60) respectively. The contours are drawn by the brush tool in photoshop with 22 pixels width while disabling the brush smoothing option. A new jpg image file is created for each slice after marking the contours, eliminating the debris, and positioning the slice in the center of the image (see Fig 22)

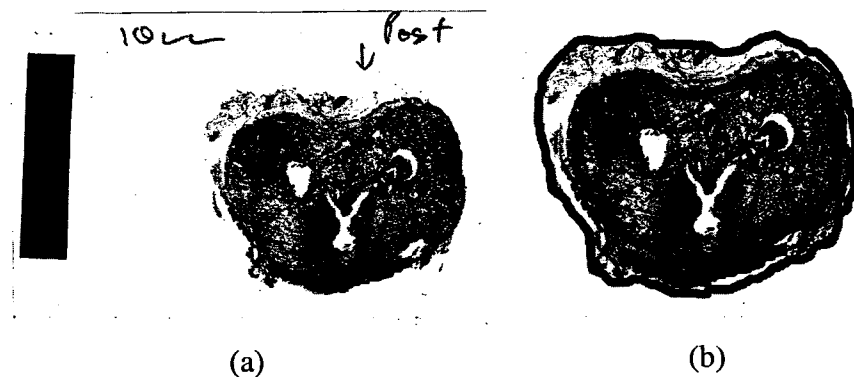
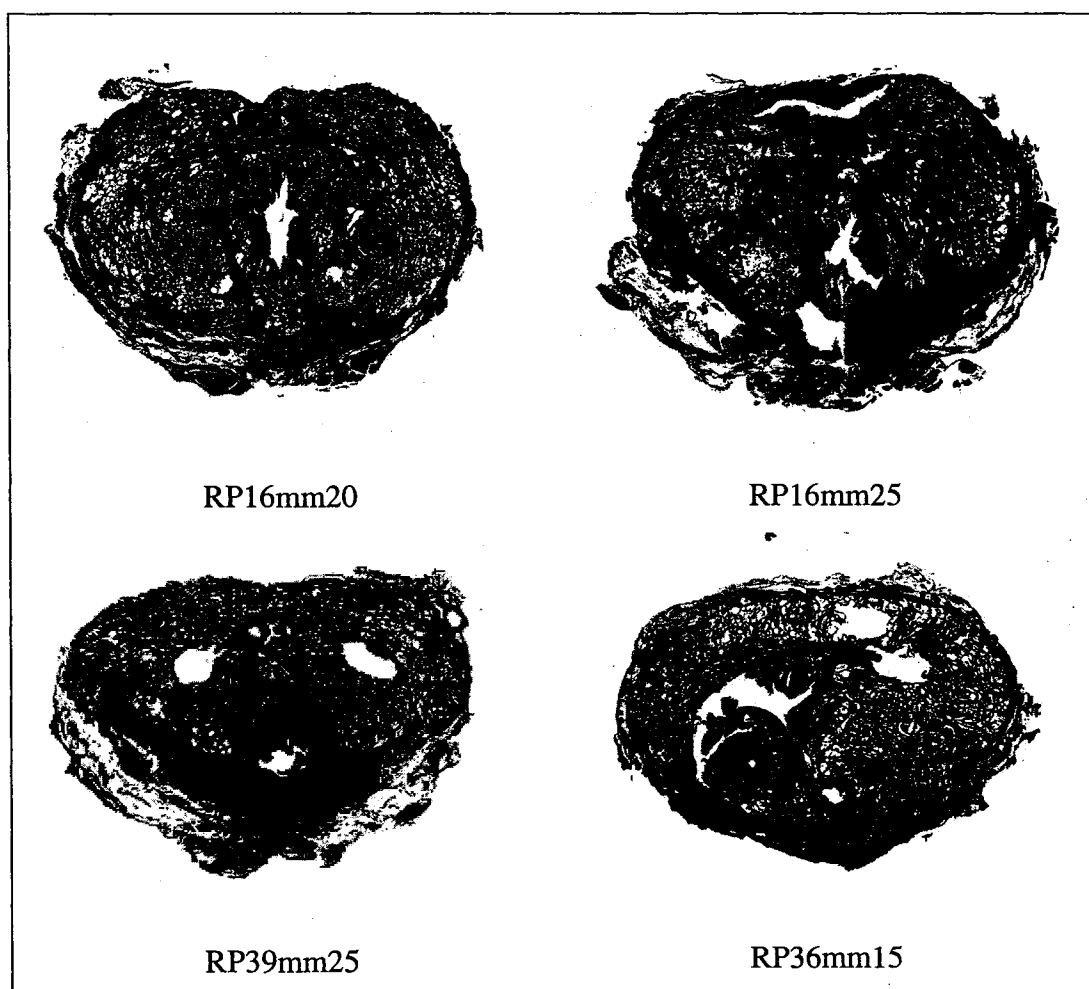


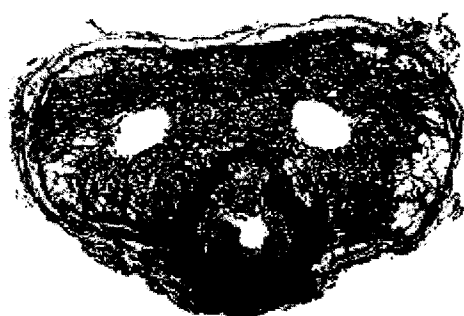
Fig 22. Slice Image (a) original slice image, (b) a processed image

5.2 Test bed

In testing our algorithms, we have used 13 images of slices cut at 5, 10, 15, 20, 25, and 30mm from the apex (Table 2). The samples are named as RP[xx]mm[yy] where xx stands for a sample number and yy stands for the distance in mm from the apex where this sample was cut.

Table 2 Test bed.





RP37mm15



RP38mm10



RP40mm10



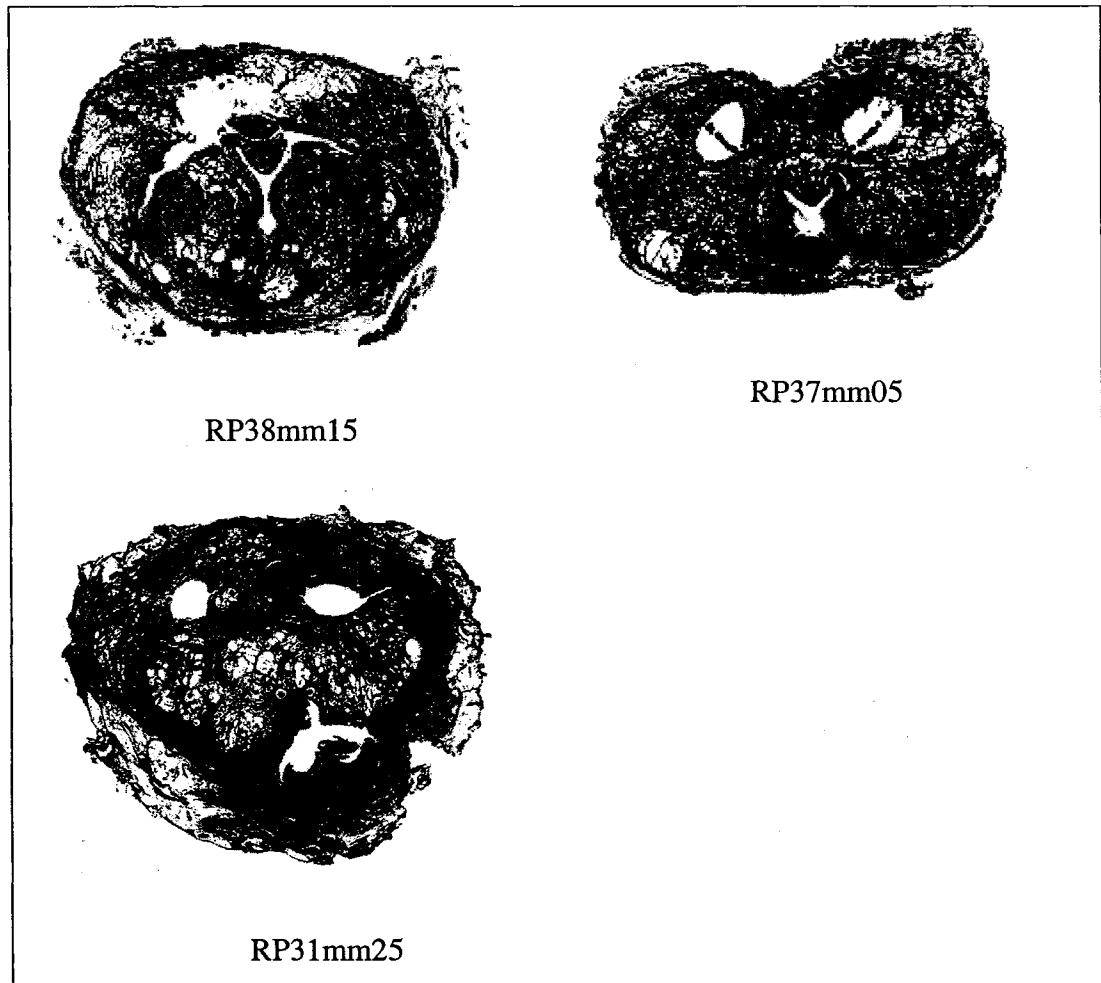
RP36mm05



RP38mm30



RP37mm10



5.3 Testing

We have tested the Generalized Hough Transform (GHT) algorithm and the least squares fitting algorithm on Pentium 4 machines, with dual processors of 3.4GHz and 1.00 GB of RAM. The 13 slices are used to test each algorithm using 3 different shape equations: the limaçon (discussed in chapter 4), the circle, and the ellipse.

The limaçon equation has 3 parameters a , b , and θ that changes the curvature, the width, and the orientation of the curve respectively. The program searches in a predetermined range of values of the parameters for the best shape that fit the slice in process. For example, in Fig 23a, the slice has a flat top so the curvature is minimal while in Fig 23b, the slice has a concave top which requires some curvature at the top.

Therefore, the limaçon generates two different shapes as shown by the arcs to accommodate each case.

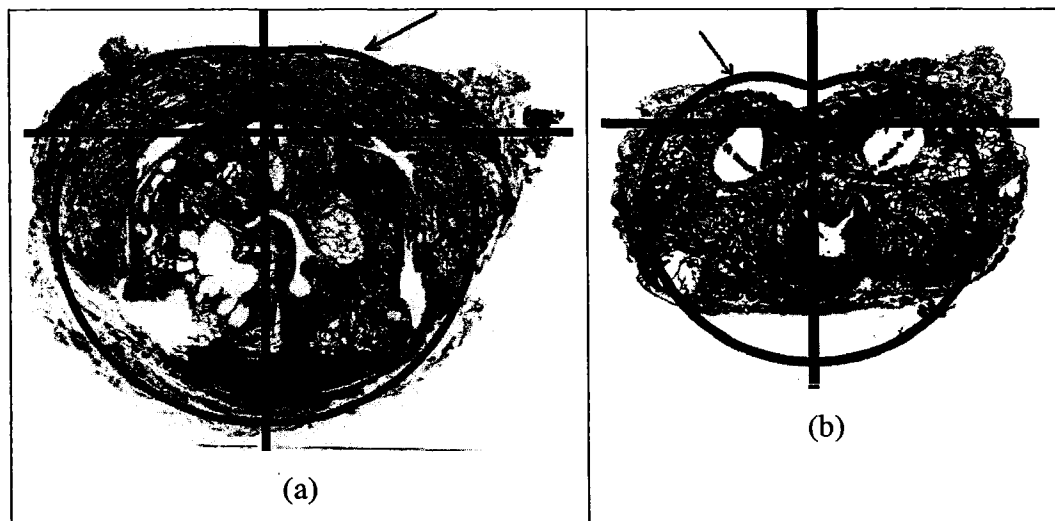


Fig 23. Limaçon curve generated for two different slices.

The input to the least squares as well as the GHT algorithms are arcs that represent the parts of the capsule that are present in the slice and can be clearly seen under the microscope or with high scanning resolution. We have assumed that these parts have already been determined by a texture based algorithm, as we explained in chapter 4, and thus we have manually drawn them for testing our algorithm. As was explained by a pathologist, we have drawn the capsule parts in areas that are close to fat tissues as shown in the Fig 24



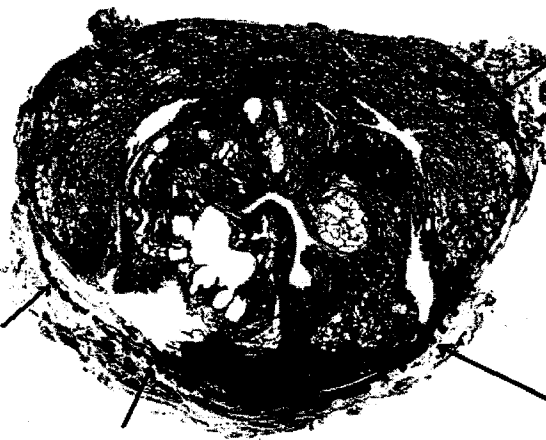
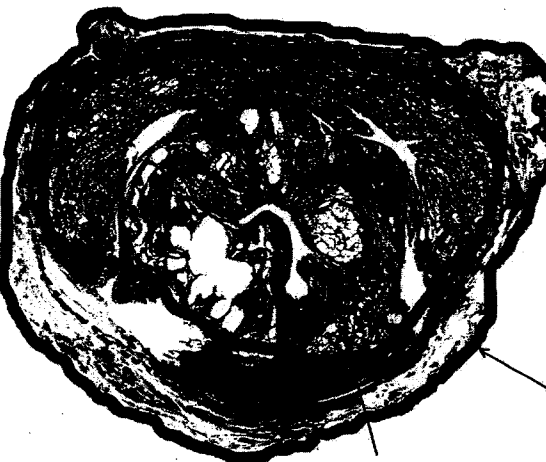
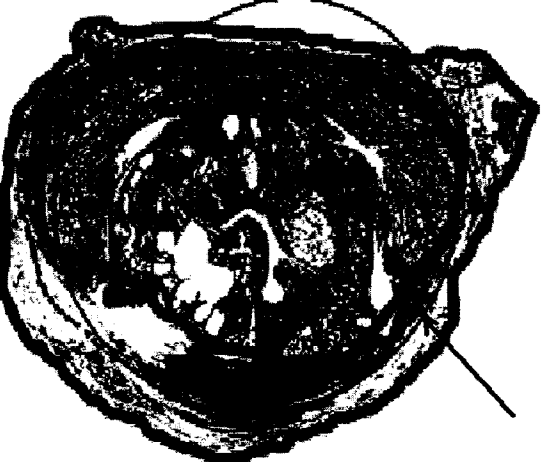
Fig 24. Manual marking of the capsule parts that are present in the slice.

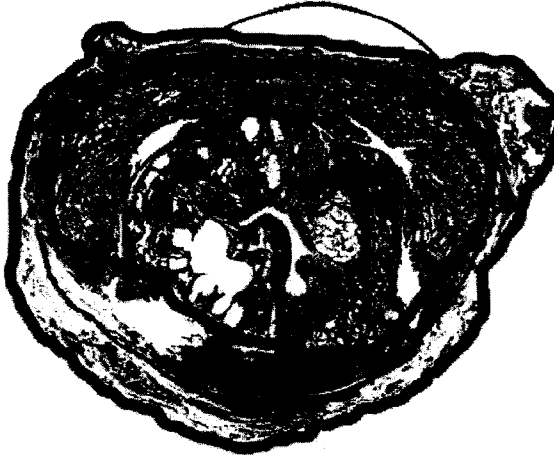
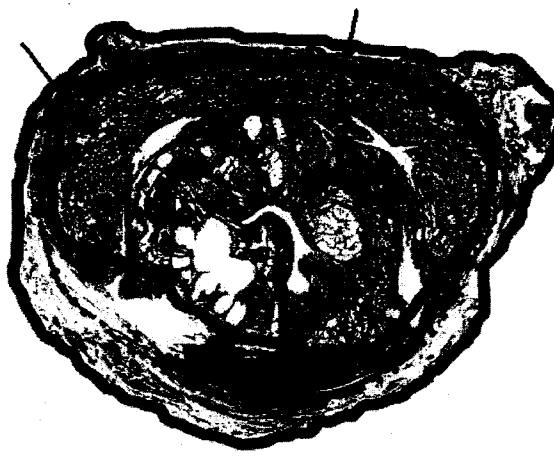

5.3.1 Testing Least squares algorithm



In chapter 4, we have explained the steps of the least squares algorithm using the limaçon equation. In this section, we show the results of applying this algorithm on our test bed using the limaçon, circle, and ellipse equations. In the following table, we show the detailed steps of running the least squares algorithms on slice RP38mm30.

Table 3: Detailed steps of applying least squares algorithm on a slice

	<p>Original image of a slice cut at 30mm from the apex. The dashed curve, manually drawn by a pathologist, shows the expected capsule.</p>
--	--

	<p>The locations where the capsule parts are present are marked and saved</p>
	<p>The parenchymal contour and the slice perimeter are marked with 2 distinct colors</p>
 <p>1st run</p>	<p>The least squares algorithm finds the best value for the equation parameters to position the output curve close to the input arcs. The arrow points to the generated curve.</p>

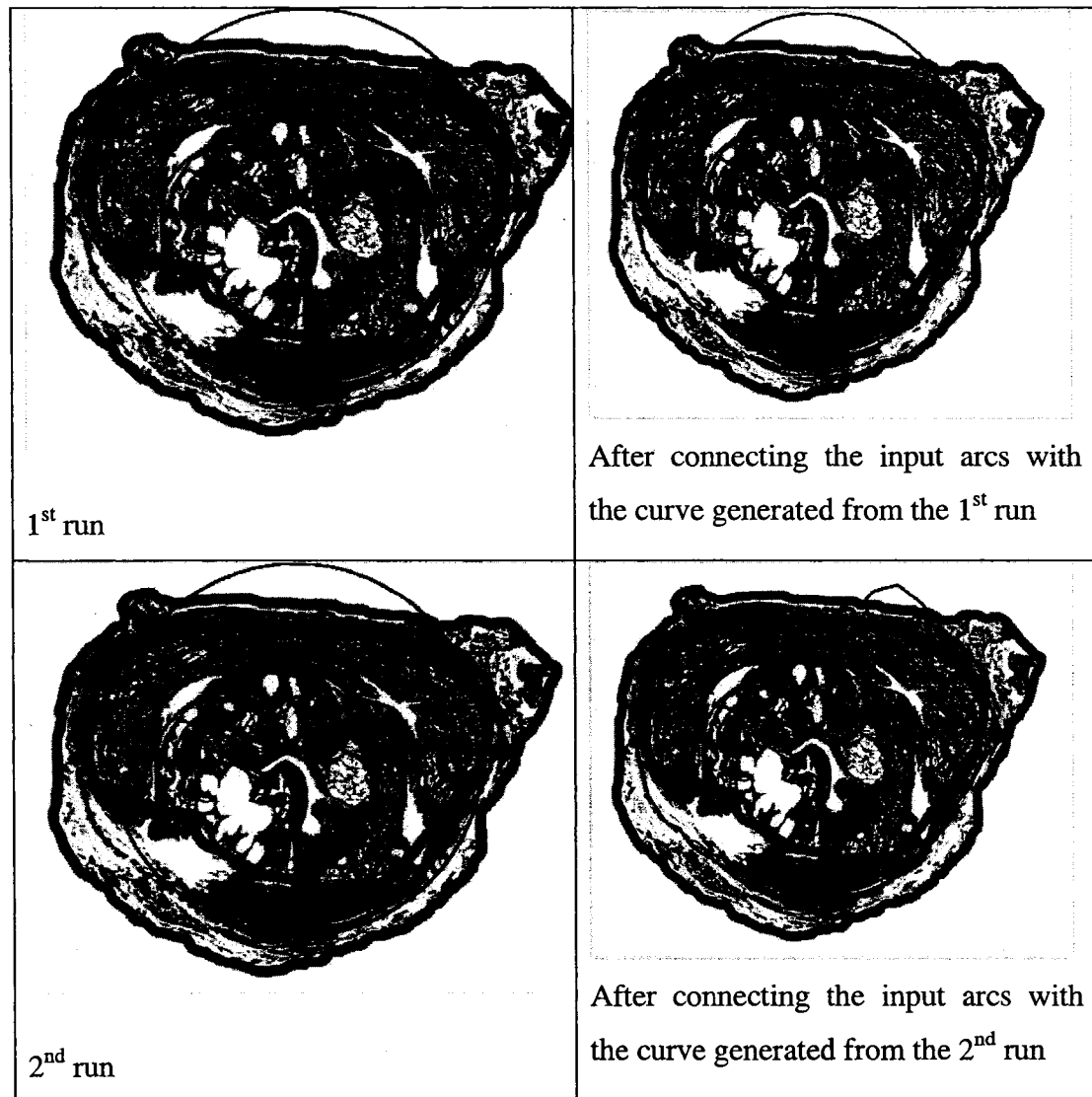
	<p>The generated curve is connected by the input arcs.</p>
	<p>Some parts of the generated curve violate the constraint which states that the capsule should be located between the parenchymal contour and the slice perimeter. Therefore we use the floodfill algorithm to relocate the points of the curve that violate the constraint and place them between the 2 contours. The new generated points are shown.</p>
 <p>2nd run</p>	<p>The algorithm runs for a second time with the original arcs as input in addition to the points generated by the floodfill algorithm in the previous step. The algorithm finds the best values (from a specific range) for the equation parameters that place the curve close to the arcs and the points.</p>

	<p>The generated curve is connected by the original input arcs as well as with the new additional points. Note that the curve doesn't violate any constraints so the floodfill will not generate any new points and therefore, the curve has converged to its optimum state.</p>
	<p>The final curve.</p>

In the example shown in Table 3, the curve has converged at the second run of the algorithm because the shape equation used is best suited for this particular slice. However, this may not be the case when the shape equation is not appropriate for the slice in process. In such a case, the algorithm can continue running further as long as the floodfill generates new points at the end of each run and the curve will converge to its optimum state eventually. However, if the shape is not good for the slice, the final curve may reach its optimum state with a high deviation from the expected curve.

In Table 4 we show the output of 2 runs for the slice explained in table using circle shape equation and in fig we show the output of 2 runs using an ellipse equation.

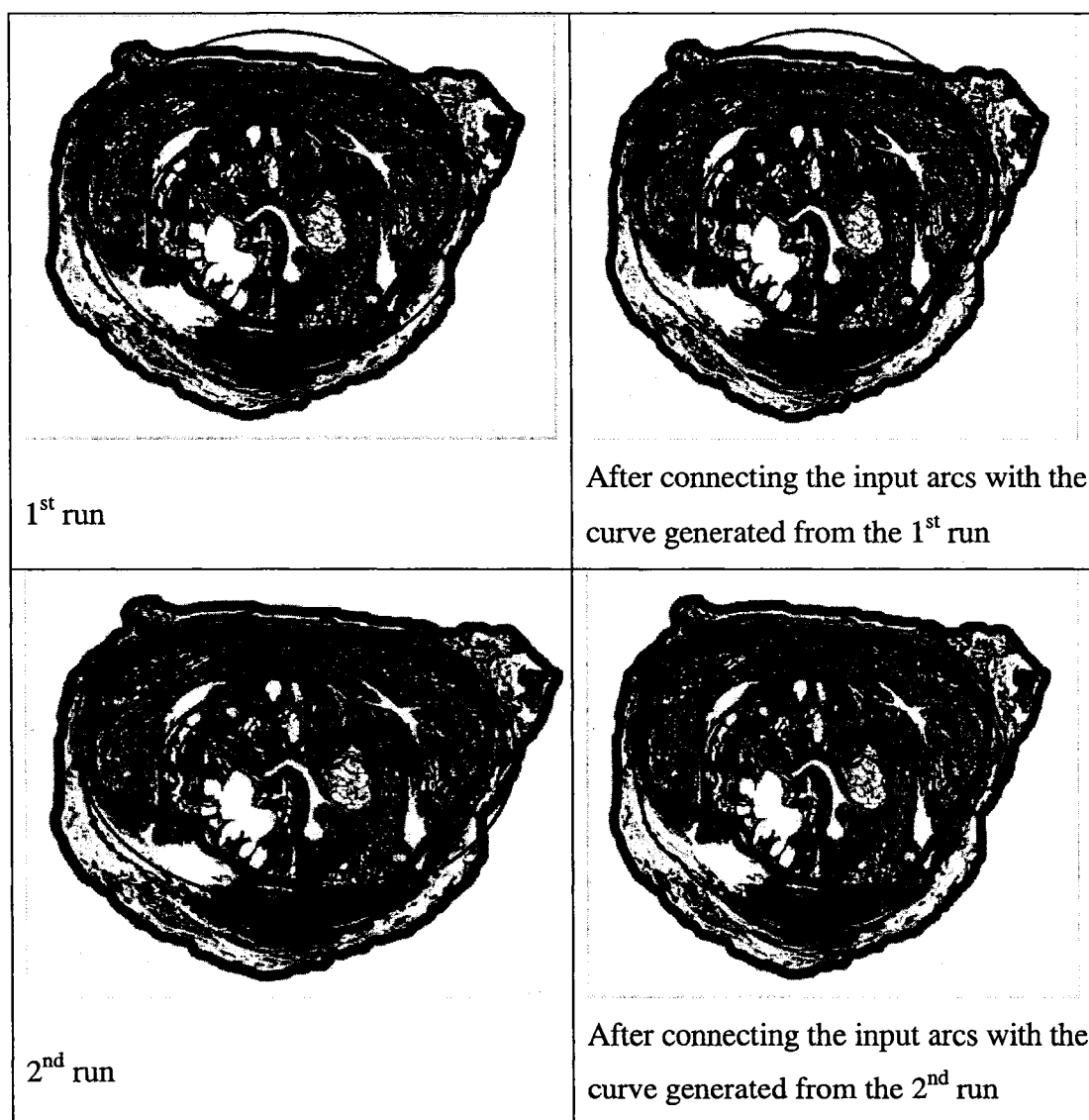
Table 4: Results of running the least squares algorithm on RP38mm30 using circle equation



From Table 4, we notice that the curve has not converged at the second run as was the case when the limaçon equation was used. However, since part of it violates

the constraint, the floodfill will push the points in between the two contours and it may converge at the 3rd run.



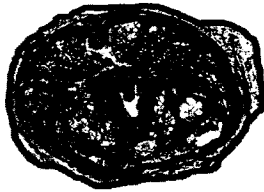


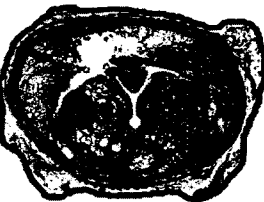

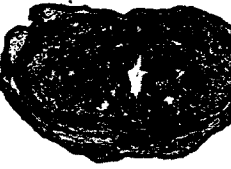
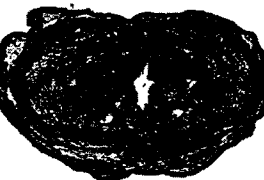


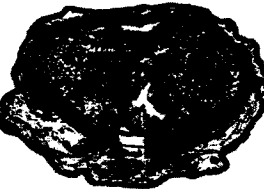
Table 5: Results from running the least squares algorithm on RP38mm30 using ellipse equation.

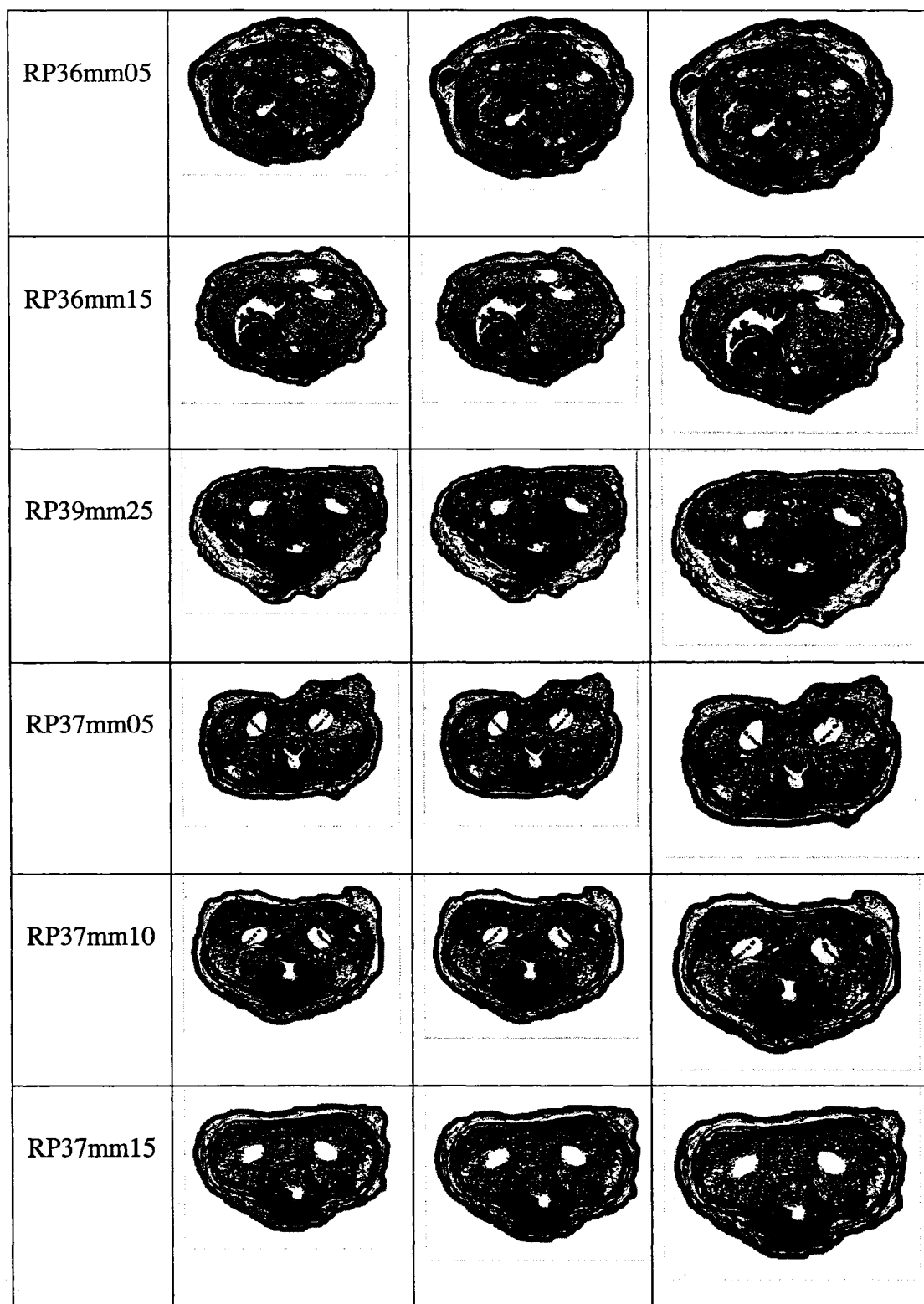


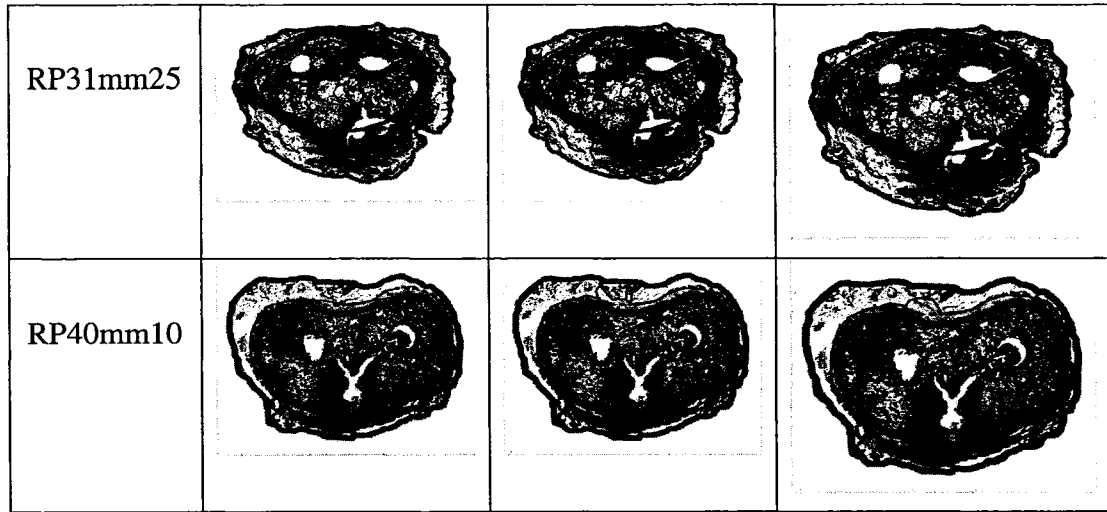
From Table 5, we notice that the curve has converged at the 2nd run as was the case when limaçon equation was used. However, the curve generated by the limaçon is closer to the expected optimum curve than the one generated by the ellipse

equation. This means that for this particular slice, the limaçon equation better suits it than the circle or the ellipse. Each of the three curve equations may be good for some slices and bad for others as shown in Table 6.

Table 6: Least squares algorithm results after the 2nd run.

Sample number	2 nd run using circle equation	2 nd run using limaçon equation	2 nd run using ellipse equation
RP38mm10			
RP38mm15			
RP16mm20			
RP16mm25			





5.3.2 Testing GHT algorithm

In this section, we show the results of applying the GHT algorithm on our test bed using the limaçon, circle, and ellipse equations. The difference between the GHT approach and the least squares approach is that in GHT we do not merge the input arcs with the generated curve after each run. The GHT uses the shape equation and tries to pass by as many points as possible of the input arcs. We have set a threshold at which we consider the curve passing by a particular point if the point is within n pixels distance from that curve. The number of pixels n is calculated by

$$n = \frac{d_1}{d_2} * t$$

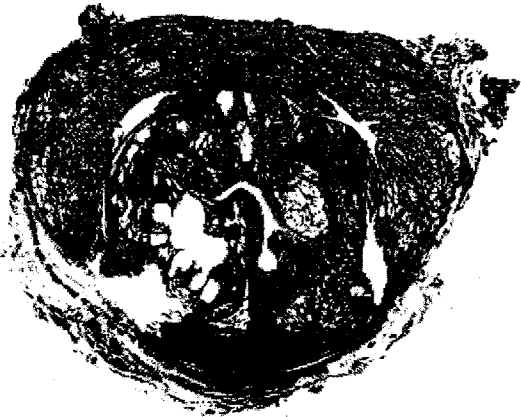
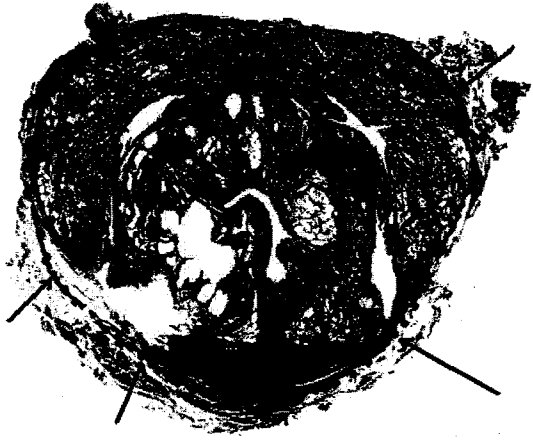
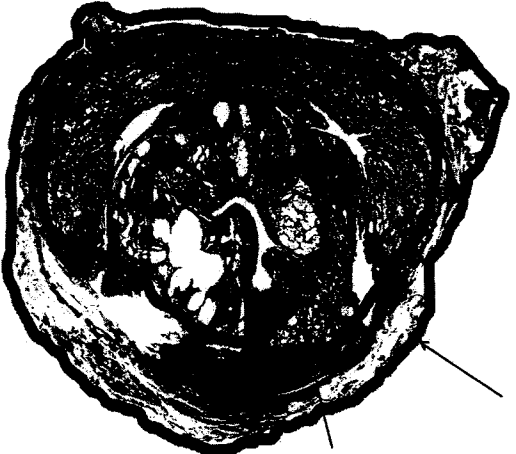
Where d_1 is the diagonal of the image in pixels,

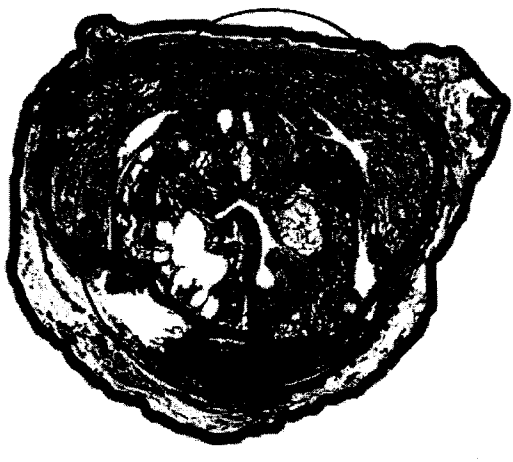


d_2 is the diagonal of the picture box of the GUI,

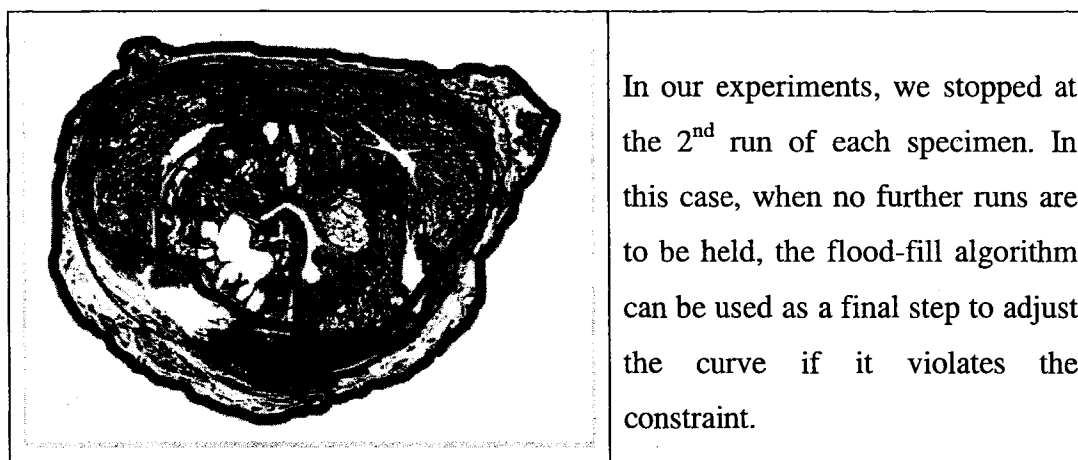
and t is a threshold that we set to 5

In the following table, we show the detailed steps of running GHT algorithms on slice RP38mm30 using limaçon equation.

Table 7: Detailed steps of applying GHT algorithm on RP38mm30.

	<p>Original image of a slice cut at 30mm from the apex. The dashed curve, manually drawn by a pathologist, shows the expected capsule.</p>
	<p>The locations where the capsule parts are present are marked and saved.</p>
	<p>The parenchymal contour and the slice perimeter are marked with 2 distinct colors.</p>

 <p>1st run</p>	<p>The GHT algorithm finds the best value for the equation parameters that enables the curve to pass by as many arc points as possible.</p>
 <p>2nd run</p>	<p>New points are generated by the floodfill algorithm for the parts where the curve has violated the bounding constraint.</p>
 <p>2nd run</p>	<p>GHT runs for a second time and the generated output curve is better than the one obtained in the 1st run. The curve still violates the bounding constraint though, therefore floodfill will generate new points and the algorithm can run for a third time.</p>



We have also applied the GHT on the same slice using circle equation and ellipse equation and the results are shown in Table 8 and Table 9 respectively.

Table 8: Results of running the GHT on RP38mm30 using circle equation.

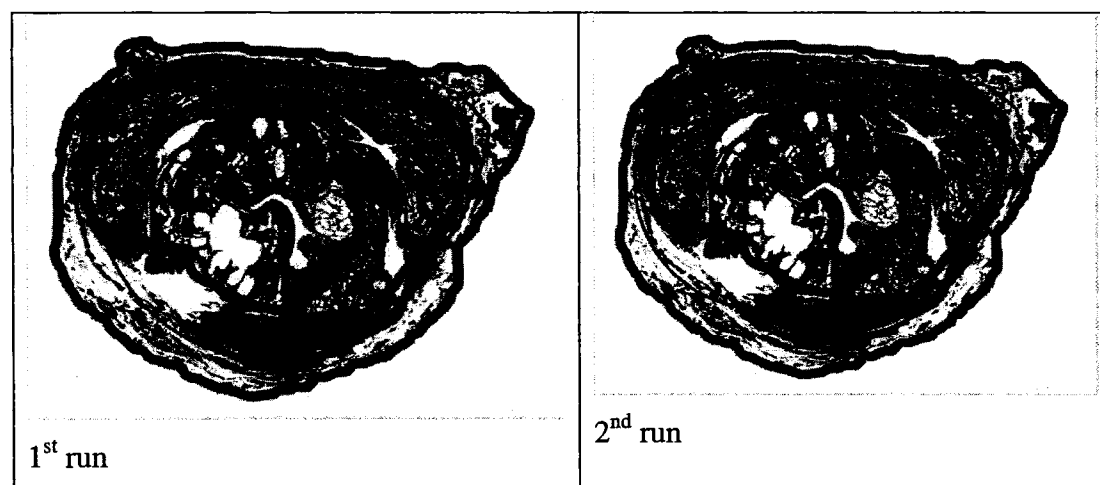
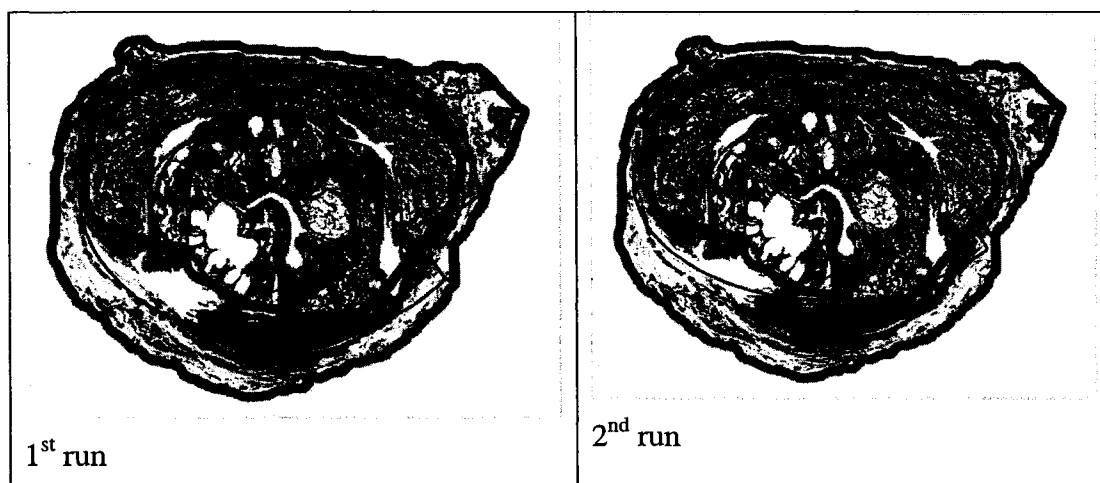

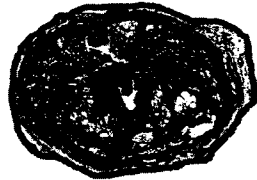



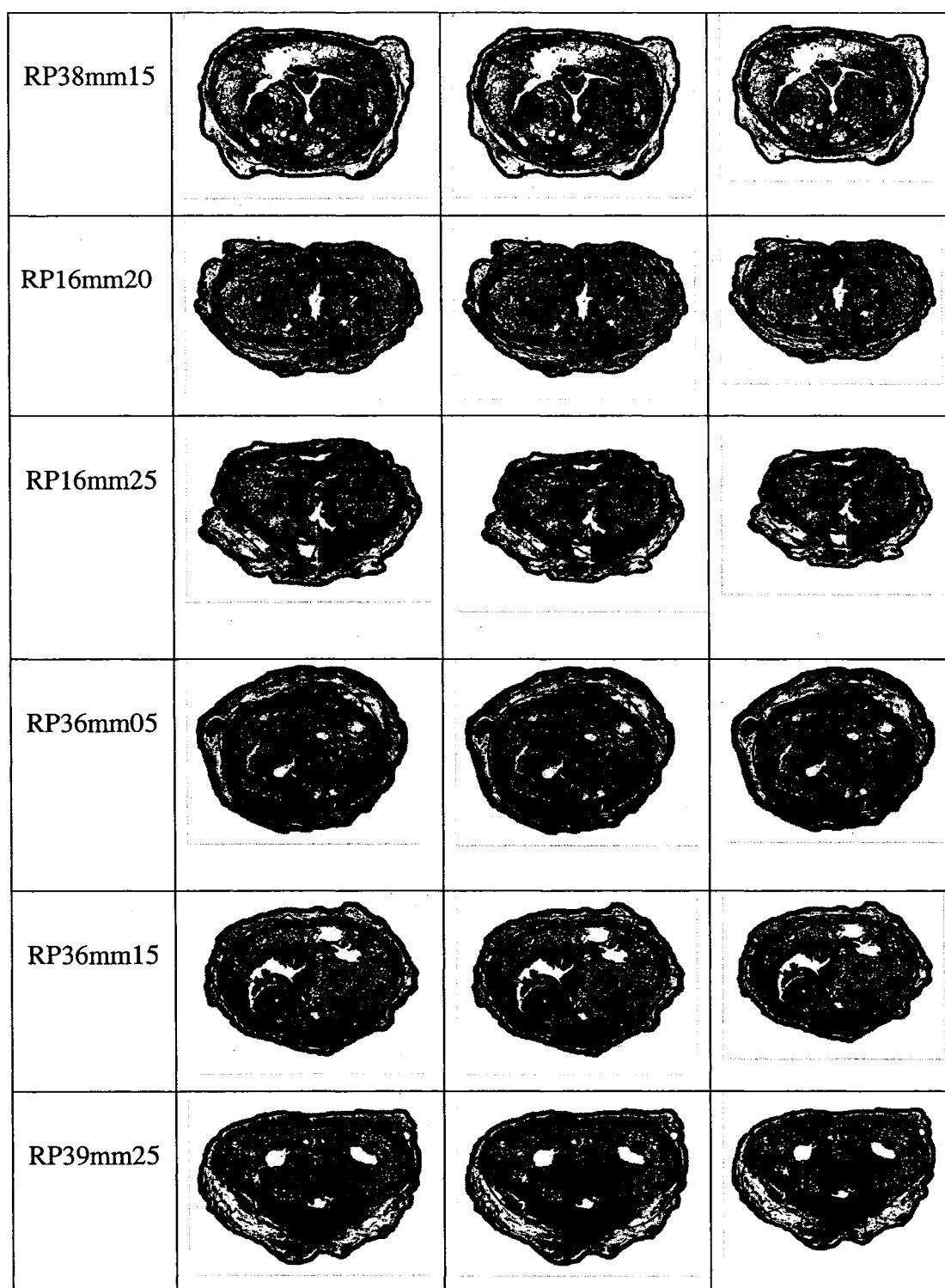
Table 9: Results of running the GHT on RP38mm30 using ellipse equation.

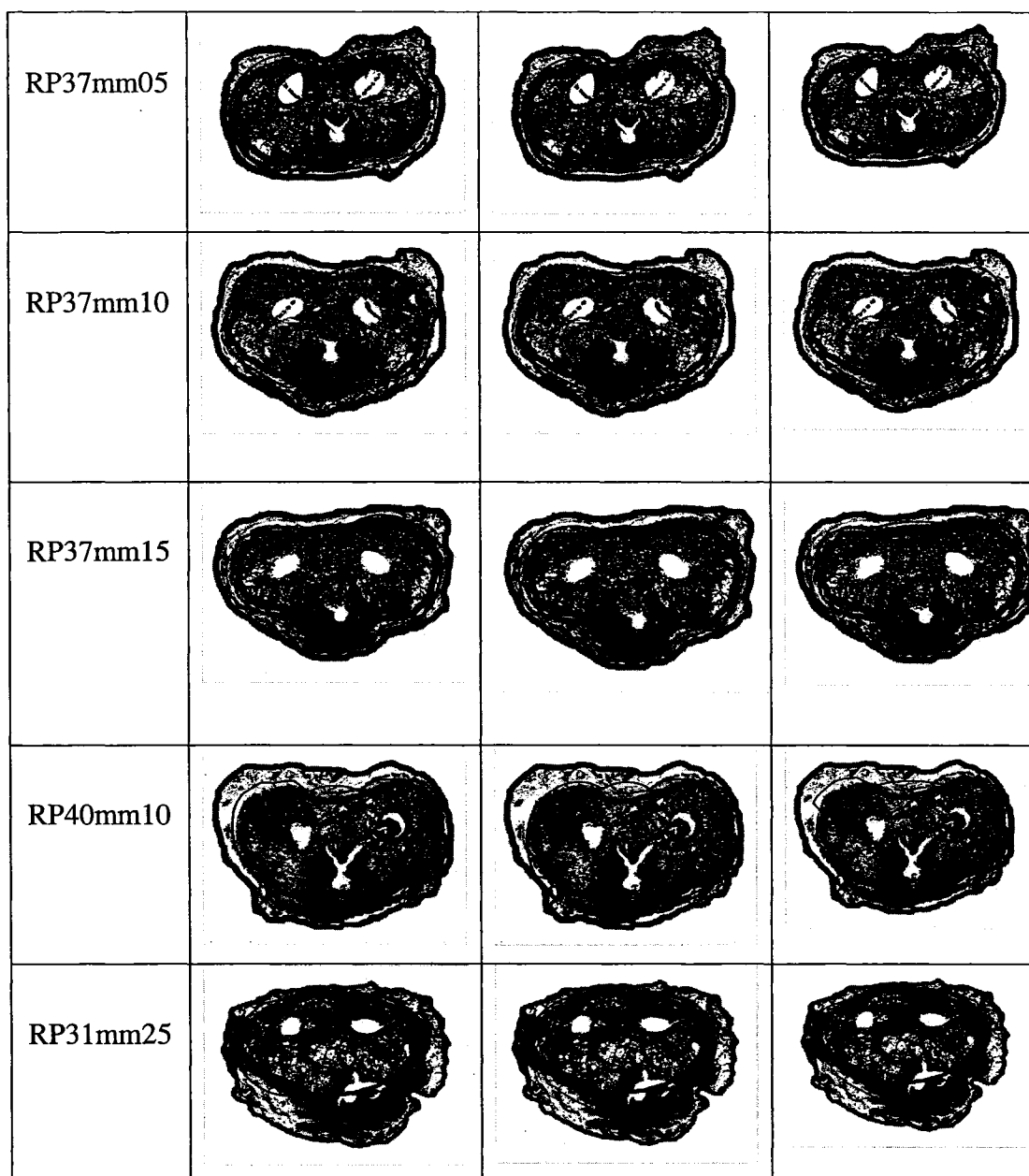


From Table 8 and Table 9, we notice that 2 runs are not enough for the GHT algorithm to converge to an optimum shape. However, at the 2nd run one can usually predict how good or bad a shape equation is for a particular slice. As the shape has more parameters that can change through the runs aiming for a best fit, the algorithm will eventually converge to an optimum curve. In the previous example, it turns out that at the second run the three shapes have produced close error percentages with the least error in the limaçon or the ellipse shape and the most in the circle shape. In the following table we show the 2nd run's results of applying GHT on our test bed using the three shape equations.

Table 10: GHT results after the 2nd run.

Sample number	2 nd run using circle equation	2 nd run using limaçon equation	2 nd run using ellipse equation
RP38mm10			





5.4 Performance evaluation

To evaluate the performance of the least squares algorithm and the GHT, we have used two measurements, the root mean square error RMSE and the percentage of error, which are defined as follows:

Root mean square error (RMSE):

Assuming that curves are represented by control points, the mean square error is the average of squared deviations. Deviations can be calculated by getting the distance from each point on the curve to the closest point on the reference curve. The root mean square error can be calculated by getting the square root of the mean square error as shown in the following equation:

$$RMS = \sqrt{\frac{\sum_{i=1}^n d_i^2}{n}}$$

Where

n is the number of points in the curve

d_i is the min distance from point i in the curve to the reference curve.

The following 2 figures shows the RMS error of the least squares algorithm and the GHT respectively

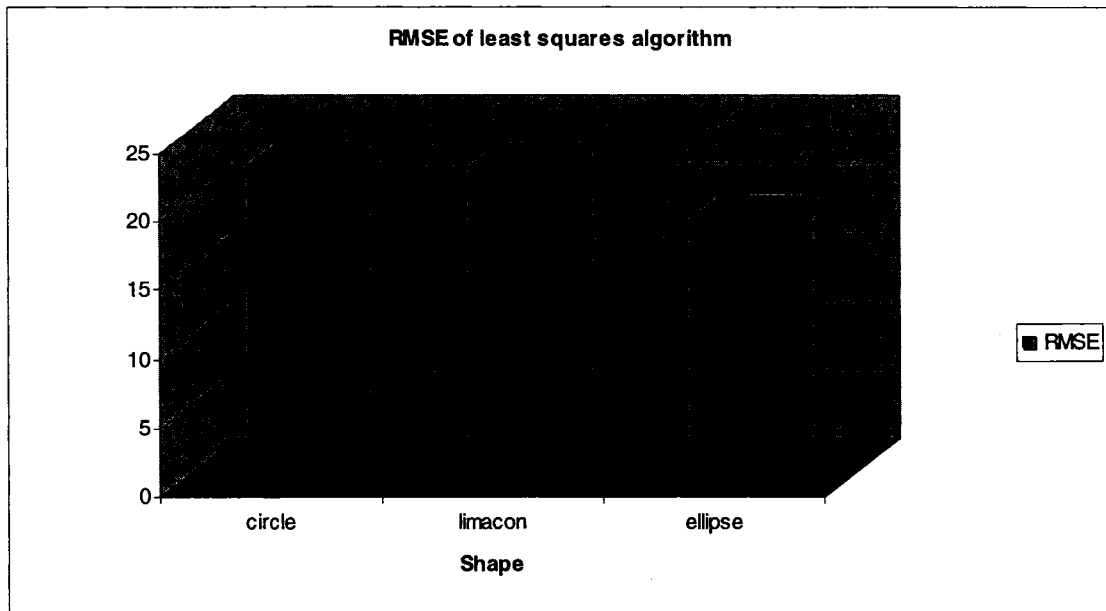


Fig 25. Root Mean Square Error for the least squares algorithm.

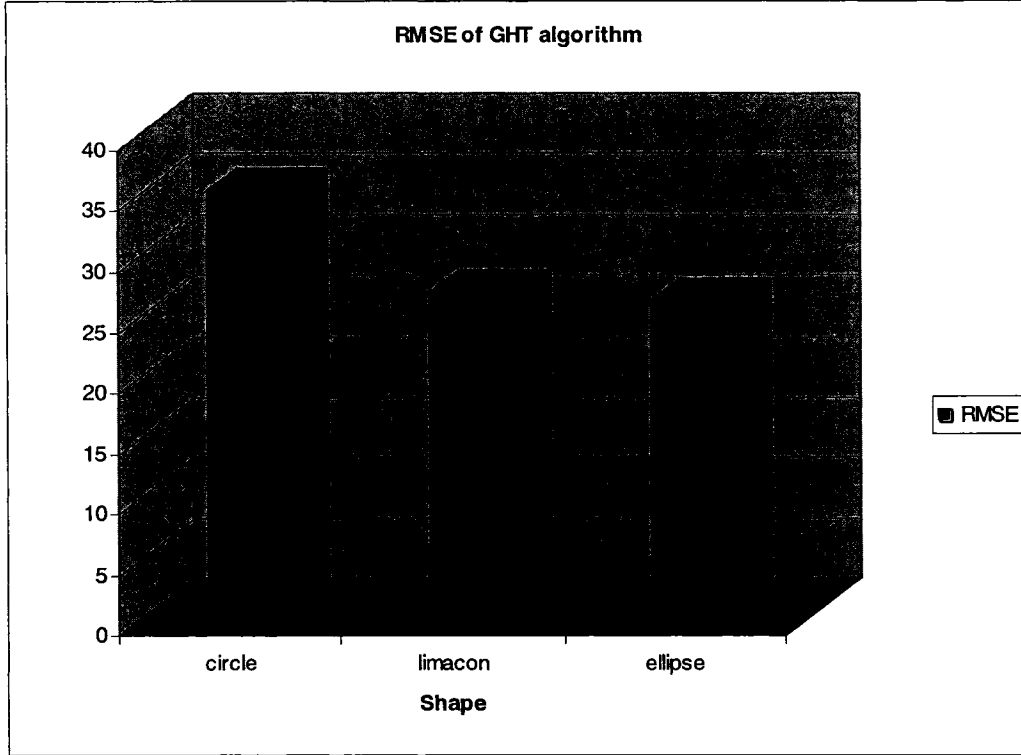


Fig 26. Root Mean Square Error for the GHT algorithm.

Percentage error:

$$\text{Percentage Error} = \sum_{i=1}^m \frac{t_i}{m}$$

Where

m is the number of points in the reference curve

$$t_i = \begin{cases} 1 & d_i > \text{threshold} \\ 0 & d_i \leq \text{threshold} \end{cases}$$

d_i is the min distance from point i in the reference curve to the curve

The thresholds considered in our study are equal to 1%, 1.5%, and 2% of the number of pixels of the image diagonal. Fig 27 illustrates the size that each threshold contributes to the actual size of a prostate slice. The squares that appear on the top left represent the number of pixels that are equal to 1%, 1.5%, 2% of the image diagonal respectively. By measuring the three squares, we found that the 2% threshold, which

is the biggest threshold we used, is less than 2mm in length. According to the fact that the capsule thickness is between 0.5 to 2mm [72], we believe that the 2% threshold is reasonable and within acceptable limits while the 1.5% threshold is used to gauge performance improvement. The 1% result is essentially directly on top of the reference line.

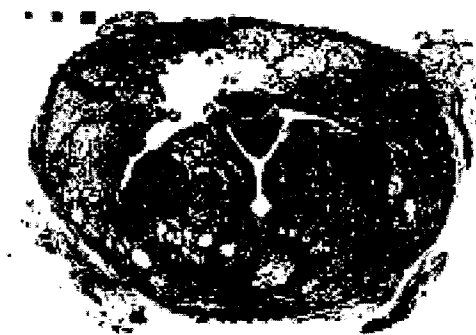
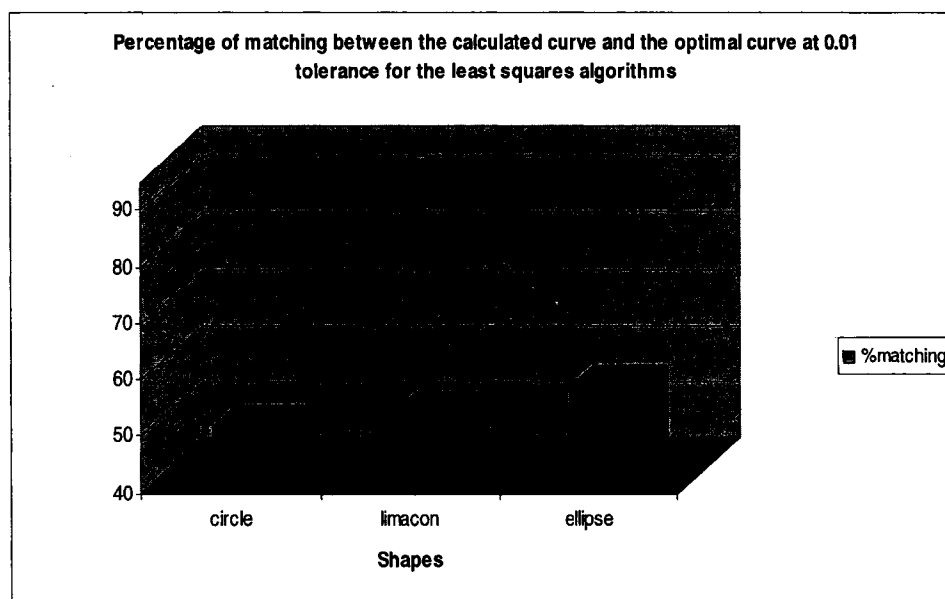


Fig 27. Thresholds with respect to an actual slice image.

The following figures show the % matching between the calculated curve and the optimal curve for the least squares and the GHT algorithms at 0.01, 0.015 and 0.02 threshold, respectively.



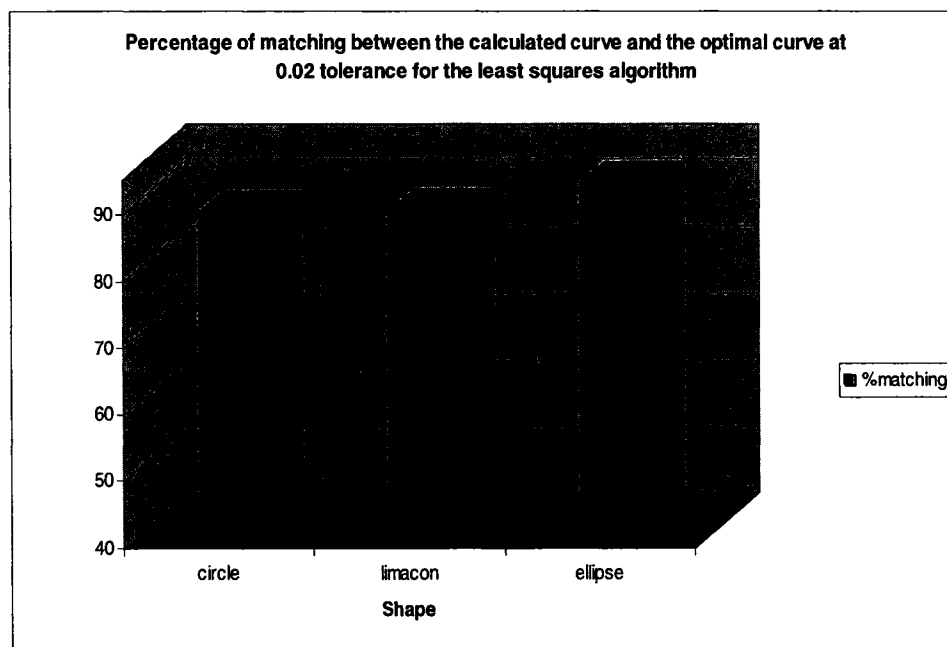
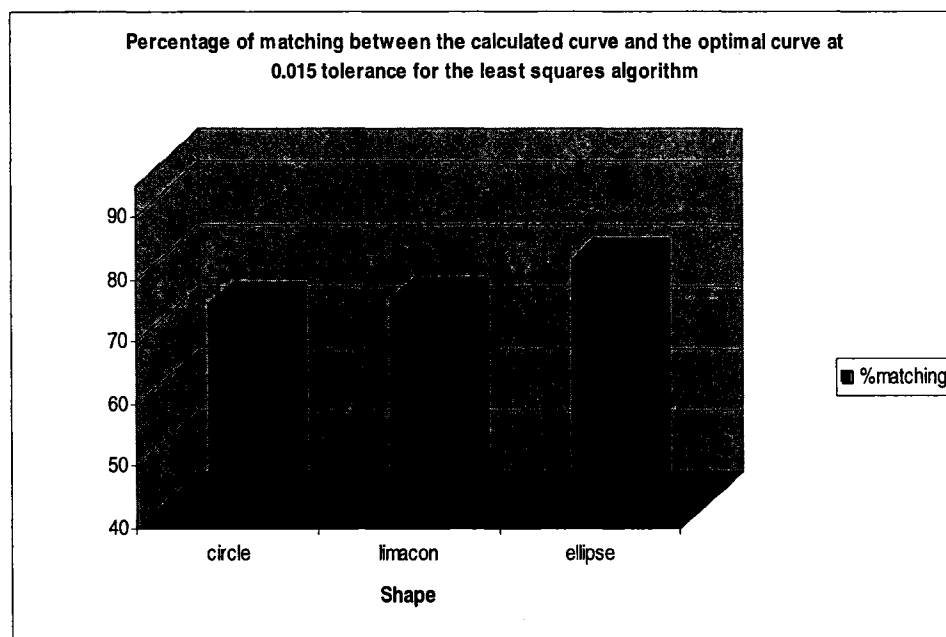
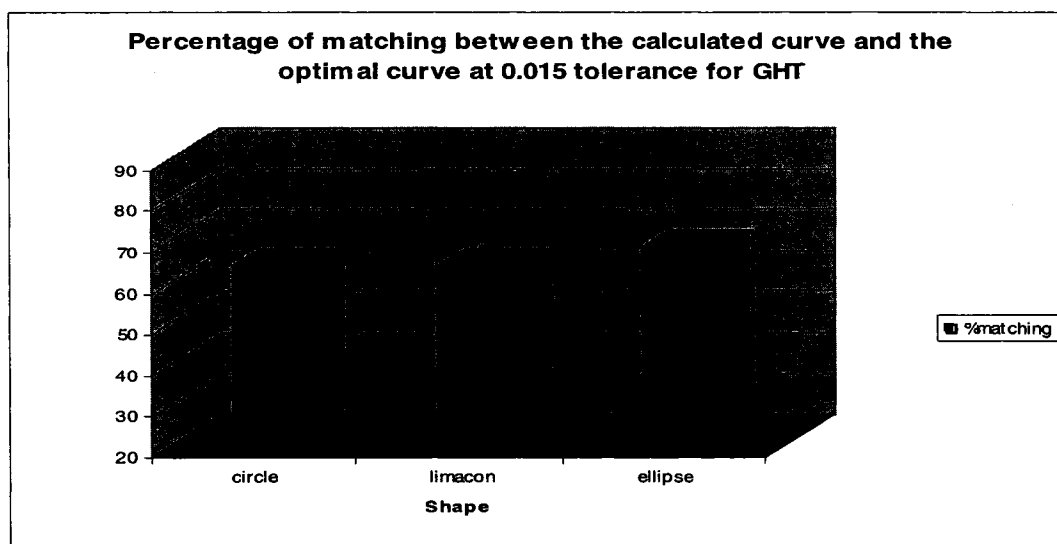
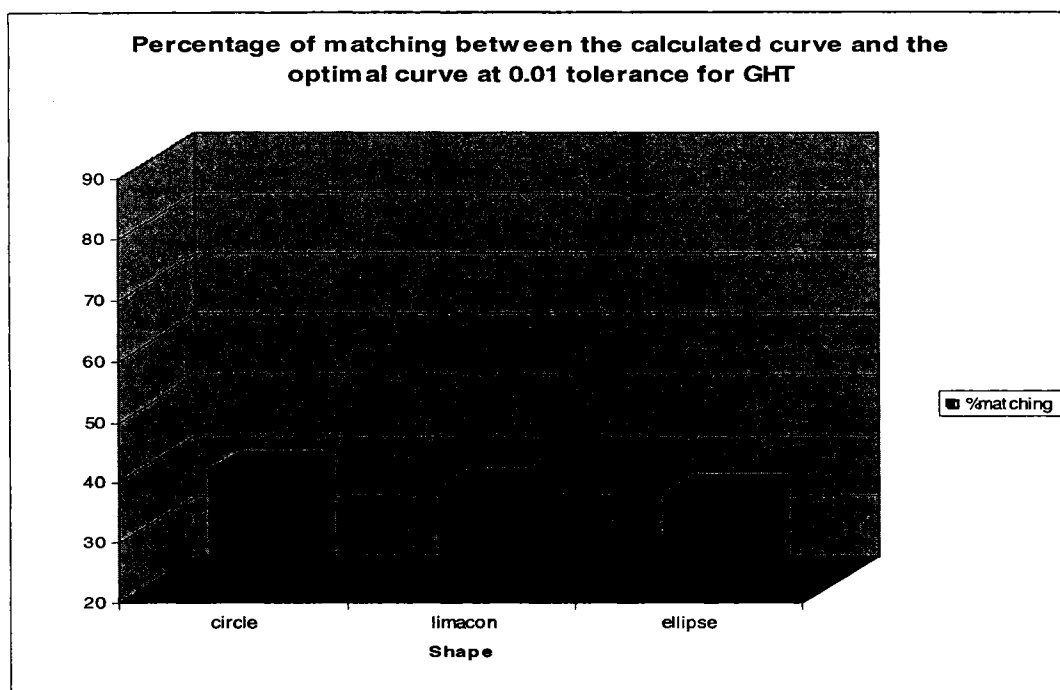


Fig 28. Percentage matching for least squares algorithm.



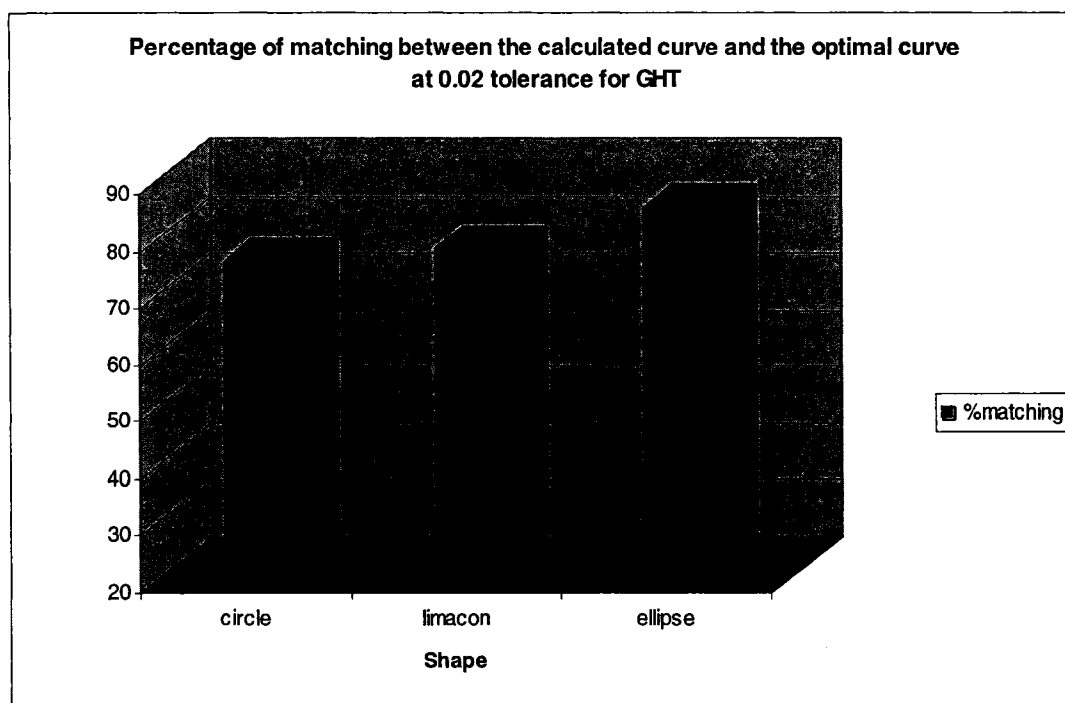


Fig 29. Percentage matching for GHT algorithm.

5.5 Discussion

The results presented in this chapter show that the GHT and the least squares shape algorithms show an aptitude for increasing capsule detection as better shape equations are used. From Table 6 and Table 10, we notice that the circle equation may produce an erroneous curve (as Table 10 shows in the case of specimens RP31mm25 and RP39mm25). This is due to the limited degree of freedom in the circle equation compared to the limaçon and ellipse equations. During experimentation we have noticed that sometimes the output curve for a particular slice gets worse after the second run of the shape algorithm (as Table 6 shows in the case of specimen RP31mm25 using limaçon equation) but gets better if we run the algorithm for a third run. The results presented in this chapter are the outcome of running the algorithms for 2 runs only; however, they can be run for as many times as needed until a satisfactory threshold is acquired. Obviously, increasing the number of runs for a particular specimen is more important for complex prostate equations that have more degrees of freedom.

We would like to point out that we used the flood-fill algorithm primarily to generate new boundary points to feed the shape algorithm for consecutive runs for better fitted output curves which also may add a smoothing effect. However, in case that one wishes to stop after a certain number of runs and the output curve extends beyond the slice perimeter or inside the parenchymal contour, the flood-fill is used as a final step to enforce these constraints. This enforcement may result in some sharp edges (as Table 10 shows in the case of RP36mm05 and RP31mm25). A curve smoothing technique can be added as a future extension to our algorithm to solve this problem.

CHAPTER VI

CONCLUSION AND FUTURE WORK

6.1 Conclusion

Despite the numerous research studies in segmenting structures from medical images and reconstructing a compact geometric representation of these structures, no study, to the best of our knowledge, has been done to automatically identify the complete prostate capsule in medical images. As studies show, identifying the prostate capsule is essential in staging prostate cancer and it greatly affects the treatment options since the presence of metastases in the prostate's adjacent organs is highly related to the penetration through the prostate capsule, which therefore influences the prognosis after surgical and hormonal treatment [50]. In addition to its importance in prostate prognosis, automatically identifying the prostate capsule provides a more accurate and objective assessment of the percentage and depth of extra-capsular soft tissue removed with the prostate by the various surgical approaches. Not only does this assessment allow surgeons to compare the quality of one surgical approach versus another, it also provides an evaluation of surgeons' surgical performances as related to a standard [49].

In this dissertation, we presented an overall process and two novel shape algorithms to detect the prostate capsule boundary with the use of Generalized Hough Transform (GHT) and least squares fitting along with prostate shape equations. We have tested our algorithms on a data set of 13 different prostate slices and our results show promises. Both algorithms show an aptitude for increasing capsule detection as better shape equations are used. The least squares algorithm used in our detection process give better results on average due to the complexity and variety of shapes analyzed. We believe that this is an artifact of the limited degrees of freedom in the shape equations used. On well behaving specimens we see that the GHT approach can do extremely well. In fact, on one specimen slice the GHT achieved zero error within our threshold. It is likely that more complex equations with greater degrees of freedom will give better results in the GHT. The combination of the two algorithms

within the overall process allows a trade off between faster processing time and smaller errors in using more complicated and flexible prostate shapes.

Given these encouraging results, the contributions of our research are:

- Creating an overall process to automatically detect the prostate capsule.
- Developing two novel shape algorithms that use Generalized Hough Transform (GHT) and least squares fitting along with prostate shape equations.
- Providing a more accurate and objective method that can be used to assess the percentage and depth of extra-capsular soft tissue removed with the prostate by the various surgical approaches. Such a method will improve assessment accuracy and reduce determination time and cost, thus replacing the current manual capsule outlining process that pathologists are tediously performing [49].

Although our research works towards a process for automatically delineating the prostate gland capsule post excision, we expect that one day it may contribute to a more accurate in-vivo segmentation approach.

6.2 Future Work

- **Automatic estimation of search parameter space**

Depending on the shape used in the curve fitting, there are various parameters that are used to obtain the most appropriate match. In least square error algorithm, the range of these parameters is varied and the error is calculated at each time. Eventually, the curve that has the least error is considered the best match. On the other hand, for the Hough technique all the possible values of parameters are tried and the number of control points passing by each curve is tracked in an accumulator. Eventually, the curve that passes by the most number of control points is selected. In either case, the selection of parameter space is crucial to the success of the applied technique to get the best curve. It is possible to estimate the lower bound and upper bound for each parameter. When using upper and lower bound for each parameter, the search space becomes very large. That in turn, makes least square technique very time consuming, and it comes at the expense of extra memory and time in Hough technique. An approach can be used to quantize the search space. However, coarse quantization leads to less accuracy, and probably failure to identify the best curve that meets the required criteria. In the future, we propose to estimate more strict boundaries on the search parameters. For example, we can limit the search space for center point to points in the inner boundary of the prostate slice. We can, based on the center point selected, determine the lower and upper bound for other parameters such as radius to ensure that the generated shapes will satisfy constraints on the generated curve.

- **Using Adaptive Hough Accumulator**

Given the fact that search space for parameters can be large, which in turn affects the memory used for the accumulator and the time to search all the space, we suggest an adaptive approach to speed up the search process and reduce the memory used in the accumulator. This can be done by predicting the lower bound and upper bound for each parameter, then using coarse quantization for the search space. Using the coarse quantization, we can have an accumulator of a very small size and the time to search that whole space will be minimal. After this process, the areas of interest

can be identified and a finer quantization can be applied to obtain more accurate results. The process can be repeated recursively until a satisfactory accuracy is acquired.

REFERENCES

- [1] "Cancer Facts and Figures 2005", *American Cancer Society*, 2005.
- [2] R. G. Aarnik, R. J. B. Giesen, A. L. Huynen, J. J. M. C. H. De La Rosete, F.M.J. Debruyne, and H. Wijkstra, "A practical clinical method for contour determination in ultrasonographic prostate images," *Ultrasound Med Biol.* vol.20, no. 7, pp. 705-717, 1994.
- [3] R.G. Aarnink, S.D. Pathak, J.J. de la Rosette, F.M. Debruyne, Y. Kim and H. Wijkstra, "Edge detection in prostatic ultrasound images using integrated edge maps," *Ultrasonics*, vol. 36 (1998) (1-5), pp. 637-644, 1998.
- [4] S. Arivazhagan, L. Ganesan, "Texture classification using wavelet transform," *Pattern Recognition Letters*, vol. 24, no.9-10, pp.1513-1521, June 2003, Publisher: Elsevier, Netherlands.
- [5] S. Arivazhagan, L. Ganesan, "Texture segmentation using wavelet transform," *Pattern Recognition Letters*, vol. 24, no.16, pp.3197-3203, Dec. 2003, Publisher: Elsevier, Netherlands.
- [6] A.G. Ayala, J.Y. Ro, R. Babaian, P. Troncoso, and D.J. Grignon, "The prostatic capsule: does it exist? Its importance in the staging and treatment of prostatic carcinoma," *Am. J. Surg. Pathol.*, vol. 13, pp. 21-27, 1989.
- [7] D. H. Ballard, "Generalizing the Hough transform to detect arbitrary shapes," *Pattern Recognition*, vol. 13, no. 2, pp. 111-122, 1981.
- [8] P. H. Bartels, H. Bartels, and R. Montironi, "Machine vision in the detection of prostate lesions in histologic sections," *Anal. Quant. Cytol. Histol.*, vol. 20, pp. 358-364, 1998.
- [9] N. Betrounia, M. Vermandela, D. Pasquierc, S. Maoucheb, and J. Rousseaua, "Segmentation of abdominal ultrasound images of the prostate using a priori information and an adapted noise filter," *Computerized Medical Imaging and Graphics*, vol. 29, pp. 43-51, 2005.
- [10] R. Bracewell, "The fourier transform and its applications," 3rd ed. *McGraw-Hill*, New York, 1999.
- [11] H. Ballentine Carter, Angelo DeMarzo, Hans Lilja, "Report to the Nation on Prostate Cancer 2004," *Medscape from WEBMD*. <http://www.medscape.com/viewprogram/3440> Release Date: September 22, 2004; Valid for credit through September 22, 2005.

- [12] G. Castellano, L. Bonilha, L.M. Li, and F. Cendes, "Texture analysis of medical images," *Clinical Radiology*, vol. 59, no. 12, Pages 1061-1069, December 2004.
- [13] B. Chiu, G.H. Freeman, M.M.A. Salama, A. Fenster, "Prostate segmentation algorithm using dyadic wavelet transform and discrete dynamic contour," *Phys. Med. Biol.*, vol. 49, pp. 4943-4960, 2004.
- [14] L.D. Cohen, "On active contour models and balloons," *CVGIP: Image Understanding*, vol. 53, no. 2, pp. 211-218, 1991.
- [15] G. Cross, and A. Jain, "Markov Random Field Texture Models", *IEEE Trans. Pattern Analysis and Machine Intelligence*, vol. 5, no. 1, pp. 25-39, 1983.
- [16] D. Cuthbert, "Fitting equations to data: computer analysis of multifactor data," 2nd edition, New York : Wiley, 1980.
- [17] R.N. Czerwinski, D.L. Jones, and W.D jr. O'Brien, "An approach to boundary detection in ultrasound imaging," *In: 1993 IEEE Ultrasonics Symposium Proceedings*. Piscataway, NJ: Institute of Electrical and Electronics Engineers; pp. 951-955, 1993.
- [18] C.A. Davatzikos, and J.L. Prince, "An active contour model for mapping the cortex," *IEEE Trans.on Medical Imaging*, vol. 14, no.1, pp. 65-80, 1995.
- [19] J. Diamond, H. Neil Anderson, Peter H. Bartels, Rodolfo Montironi, and Peter W. Hamilton, "The use of morphological characteristics and texture analysis in the identification of tissue composition in prostatic neoplasia," *Human Pathology* vol. 35, no. 9, pp. 1121-1131, September 2004.
- [20] Du-Ming Tsai, "An improved generalized Hough transform for the recognition of overlapping objects," *Image & Vision Computing*, vol. 15, no.12, pp.877-88, Dec. 1997.
- [21] L. Dzung, X. Chenyang, L. Jerry, "Current methods in medical image segmentation," *Annual Review of Biomedical Engineering*, vol. 2, pp. 315-337, 2000.
- [22] J. E. Ji, and E. Craine, "Texture analysis for classification of cervix lesions," *IEEE Trans. Med. Imaging*, vol. 19, pp. 1144-1149, 2000.
- [23] B. Van Ginneken B, S. Katsuragawa, B.M Romeny, D. Kunio, M.A. Viergever, "Automatic detection of abnormalities in chest radiographs using local texture analysis," *IEEE Transactions on Medical Imaging*, vol.21, no.2, pp.139-49, Feb. 2002.

- [24] L. Gong, S.D. Pathak, D.R. Haynor, P.S. Cho, and Y. Kim, "Parametric Shape Modeling Using Deformable Superellipses for Prostate Segmentation," *IEEE Transactions on Medical Imaging*, vol. 23, pp. 340-349, 2004.
- [25] I. Fitton, J. Shen, J.M Perron, A. Kerouani, R. Roudaut, and J.L Barat, "Regional myocardial wall thickening of the left ventricle from segmentation of echocardiographic images," *SPIE-Int. Soc. Opt. Eng. Proceedings of Spie - the International Society for Optical Engineering*, vol. 4549, pp.58-63, 2001.
- [26] E. Gelenbe, Y. Feng, K.R.R. Krishnan, "Neural network methods for volumetric magnetic resonance imaging of the human brain," *Proc. IEEE*, vol. 84, pp.1488-1496, 1996
- [27] P. Gibbs, D.L. Buckley, S.J. Blackband, A. Horsman, "Tumour volume detection from MR images by morphological segmentation," *Phys. Med. Biol.*, vol. 41, pp. 2437-2446, 1996.
- [28] L. Gupta, A. Singh, D. Geiger, C. Liang, M. Chiu, P. Adler, M. Haacke, and D. Wilson, "Cardiac MRI analysis: Segmentation of myocardial boundaries using deformable models," *Siemens Corp. Res.*, Princeton, NJ, Tech. Rep., 1995.
- [29] P.W. Hamilton, P.H. Bartels, and D. Thompson, "Automated location of dysplastic fields in colorectal histology using image texture analysis," *J. Pathol.*, vol.182, pp. 68-75, 1997.
- [30] P.W. Hamilton, P.H. Bartels, and R. Montironi, "Automated histometry in quantitative prostate pathology," *Anal. Quant. Cytol. Histol.* vol. 20, pp. 443-460, 1998.
- [31] R. Haralick, "Statistical and Structural Approaches to Texture", *Proc. IEEE*, vol. 67, no. 5, pp. 786- 804, 1979.
- [32] R.M. Haralick, L.G. Shapiro, "Image segmentation techniques," *Comput. Vis. Graph. Image Proc.*, vol. 29, pp.100-132, 1985.
- [33] D. Hearn, M.P. Baker, "Computer Graphics", *Prentice Hall Inc.*, 1994.
- [34] R. Hussein, F. McKenzie, R. Joshi, "Automating prostate capsule contour estimation for 3D model reconstruction using shape and histological features," *SPIE-Int. Soc. Opt. Eng. Proceedings of SPIE* vol. 5367, no.1, pp.790-798, 25 May 2004, USA.
- [35] N. Karssemeijer, "Automated classification of parenchymal patterns in mammograms," *Physics in Medicine & Biology*, vol. 43, no. 2, pp.365-78. Publisher: IOP Publishing, UK, Feb. 1998.

- [36] M. Kass, A. Witkin, D. Terzopoulos, "Snakes: active contour models," *Int. J. Comput. Vision*, vol. 1, pp. 321-331, 1987.
- [37] C. Knoll, M. Alcaniz, V. Grau, C. Monserrat and M.C. Juan, "Outlining of the prostate using snakes with shape restrictions based on the wavelet transform," *Pattern Recogn.* vol. 32, no. 10, pp. 1767-1781, 1999.
- [38] C. Knoll, M. Alcaniz, C. Monserrat, V. Grau and M.C. Juan, "Multiresolution segmentation of medical images using shape-restricted snakes," *Proc. SPIE*, vol. 3661, pp. 222-233, 1999.
- [39] H.M. Ladak, F. Mao, Y. Wang, D.B. Downey, D.A. Steinman and A. Fenster, "Prostate segmentation from 2D ultrasound images," *Med. Phys.*, vol. 27, pp. 1777-1788, 2000.
- [40] Y.J. Liu, W.S. Ng, M.Y. Teo, and H.C. Lim, "Computerised prostate boundary estimation of ultrasound images using radial bas-relief method," *Med. Biol. Eng. Comput.*, vol. 35, no. 5, pp. 445-454, 1997.
- [41] Y.J. Liu, W.S. Ng, M.Y. Teo and H.C. Lim, "Computerised prostate boundary estimation in ultrasound images using the radial bas-relief method," *Med. Biol. Eng. Comput.*, vol. 35, pp. 4450-4454, 1997.
- [42] A. Lorenz, C. Haas and H. Ermer, "Segmentation of ultrasonic prostate images using a probabilistic model based on markov random processes," *Ultrason. Imaging*, vol. 19, pp. 44-45, 1997.
- [43] C. Lu, P. Chung, and C. Chen, "Unsupervised Texture Segmentation via Wavelet Transform", *Pattern Recognition*, vol. 30, no. 5, pp. 729-742, 1997.
- [44] S. Mallat, "Multifrequency Channel Decomposition of Images and Wavelet Models," *IEEE Trans. Acoustic, Speech and Signal Processing*, vol. 37, no. 12, pp. 2091-2110, 1989.
- [45] A. Madabhushi, M. Feldman, D. Metaxas, D. Chute, J. Tomaszewski, "Optimal feature combination for automated segmentation of prostatic adenocarcinoma from high resolution MRI," *Proceedings of the 25th Annual International Conference of the IEEE Engineering in Medicine and Biology Society (IEEE Cat. No.03CH37439). IEEE. Part* vol.1, pp.614-17, Piscataway, NJ, USA, 2003.
- [46] K.A. Marghani, S.S. Dlay, B.S. Sharif, and A.J. Sims, "Automated morphological analysis approach for classifying colorectal microscopic images," *SPIE-Int. Soc. Opt. Eng. Proceedings of SPIE - the International Society for Optical Engineering*, vol.5267, no.1, pp.245-54, 1 Oct. 2003, USA.

- [47] A. Materka, M. Strzelecki, "Texture analysis methods: a review," Technical University of Lodz, Poland: COST B11Report; 1998. http://www.eletel.p.lodz.pl/cost/pdf_1.pdf.
- [48] T. McInerney, and D. Terzopoulos, "Deformable models in medical images analysis: a survey," *Medical Image Analysis Journal*, vol. 1, pp. 91–108, 1996.
- [49] F. D. McKenzie, R. Hussein, J. Seevinck, P. Schellhammer, and J. Diaz. "Prostate Gland and Extra-Capsular Tissue 3D Reconstruction and Measurement," *The 3rd IEEE symposium on Bioinformatics and Bioengineering (BIBE)*, Bethesda, Maryland, pp. 246-250, March 10-12, 2003.
- [50] J.E. McNeal, A.A. Villers, E.A. Redwine, F.S. Freiha, and T.A. Stamey, "Capsular penetration in prostate cancer: significance for natural history and treatment," *Am. J. Surg. Pathol.*, vol. 14, pp. 240-247, 1990.
- [51] J.J. Mi, B. Lee, H. Choi, H. Hwang, S. Nam, H. Choi, "Development of fitting model for visualization of left ventricle in gated SPECT image using least squares method," *Proceedings of 7th International Workshop on Enterprise Networking and Computing in Healthcare Industry. HEALTHCOM 2005 (IEEE Cat. No. 05EX1016)*. IEEE, pp. 396-9. Piscataway, NJ, USA, 2005.
- [52] I. Middleton, R.I. Damper, "Segmentation of magnetic resonance images using a combination of neural networks and active contour models," *Med. Eng. Phys.*, vol. 26, no.1, pp.71-86, 2004.
- [53] I. P. Nedzved, "Morphological Segmentation of Histology Cell Images," *IEEE ICPR'00*, vol.1, pp.1500, 2000.
- [54] N.R. Pal, S.K. Pal, "A review on image segmentation techniques," *Pattern Recognit.*, vol. 26, pp.1277–1294, 1993.
- [55] S.D. Pathak, R.G. Aarnink, J.J. de la Rosette, V. Chalana, H. Wijkstra, F.M.J. Debruyne and Y. Kim, "Quantitative three-dimensional transrectal ultrasound for prostate imaging," *Proc. SPIE*, vol. 3335, pp. 83–92, 1998.
- [56] S.D. Pathak, D.R. Haynor, and Y. Kim, "Edge-guided boundary delineation in prostate ultrasound images," *IEEE Transactions on Medical Imaging*, vol.19, no.12, pp.1211-19. Publisher: IEEE, USA, Dec. 2000.
- [57] Pentland, "Fractal-Based Description of Natural Scenes," *IEEE Trans. Pattern Analysis and Machine Intelligence*, vol. 6, no. 6, pp. 661-674, 1984.

- [58] S. Petushi, C. Katsinis, C. Coward, F. Garcia, and A. Tozeren, "Automated identification of microstructures on histology slides," *2nd IEEE International Symposium on Biomedical Imaging: Macro to Nano (IEEE Cat No. 04EX821)*. IEEE, vol. 1, pp. 424-471. Piscataway, NJ, USA, 2004.
- [59] M. Pilu, A.W. Fitzgibbon, R.B. Fisher, "Ellipse-specific direct least-square fitting," *Proceedings. International Conference on Image Processing (Cat. No.96CH35919)*. IEEE. vol.3, pp. 599-602, New York, NY, USA, 1996.
- [60] B.W. Pogue, M.A. Mycek, D. Harper, "Image analysis for discrimination of cervical neoplasia," *Journal of Biomedical Optics*, vol.5, no.1, pp.72-82. Publisher: SPIE, USA, Jan. 2000.
- [61] S. Pohlman, K.A. Powell, N.A. Obuchowski, W.A. Chilcote, and S.G. Broniatowski, "Quantitative classification of breast tumors in digitized mammograms," *Med. Phys.*, vol. 23, pp.1337-1345, 1996.
- [62] J.S. Prater, W.D. Richard, "Segmenting ultrasound images of the prostate using neural networks," *Ultrason. Imag.*, vol. 14, pp. 159-185, 1992.
- [63] S. Pui-Kin and S. Wan-Chi, "A new generalized Hough transform for the detection of irregular objects," *Journal of Visual Communication & Image Representation*, vol. 6, no.3, pp.256-264, Sept. 1995.
- [64] S. Qian, D. Chen, "Discrete Gabor transform," *IEEE trans Signal Process*, vol. 41, pp. 2429-2438, 1993.
- [65] J. Qiang, J. Engel, and E. Craine, "Classifying cervix tissue patterns with texture analysis," *Pattern Recognition*, vol.33, no.9, pp.1561-1573. Publisher: Elsevier, UK, Sept. 2000.
- [66] S. Raganath, "Contour extraction from cardiac MRI studies using snakes," *IEEE Trans. Med. Imag.*, vol. 14, pp. 328-338, 1995.
- [67] W.E. Reddick, J.O. Glass, E.N. Cook, T.D. Elkin, and R.J. Deaton, "Automated segmentation and classification of multispectral magnetic resonance images of brain using artificial neural networks," *IEEE Trans. Med. Imaging*, vol. 16, pp.911-918, 1997.
- [68] W.D. Richard, C.G. Keen, "Automated texture-based segmentation of ultrasound images of the prostate," *Computerized Medical Imaging & Graphics*, vol.20, no.3, pp.131-140. Publisher: Elsevier, UK, May-June 1996.
- [69] A. Rosenfeld, and J. Weszka, "Picture Recognition," in *Digital Pattern Recognition*, K. Fu (Ed.), Springer-Verlag, pp. 135-166, 1980.

- [70] P.K. Sahoo, S. Soltani, and A.K.C. Wong, "A survey of thresholding techniques," *Comput. Vis. Graph. Image Proc.*, vol. 41, pp.233–260, 1988.
- [71] J. Samarabandu, R. Acharya, E. Hausmann, and K. Allen, "Analysis of bone X-rays using morphological fractals," *IEEE Transactions on medical imaging*, vol. 12, no. 3, pp. 466 – 470, Sept. 1993.
- [72] A.A. Sattar, J. Noël, J. Vanderhaeghen, C. Schulman, and E. Wespes, "Prostate capsule: computerized morphometric analysis of its components," *Urology*, vol. 46, no. 2, pp. 178-181, 1995.
- [73] P.Schellhammer, J. Diaz, F. McKenzie, R. Chaganty, and R. Hussein. "Computer modeling technology to assess extra-capsular tissue coverage of whole mount sections after retropubic and laparoscopic radical prostatectomy," *To be submitted to the Journal of Urology (Gold Journal)*, July 2006.
- [74] J. Serra, "Image Analysis and Mathematical Morphology," *Academic Press*, 1982.
- [75] R.C. Semelka, "Abdominal Pelvic MRI," *J Wiley & Sons*, New York, 2002.
- [76] F. Shao, K.V. Ling, W.S. Ng, R.Y. Wu, "Prostate boundary detection from ultrasonographic images: review article," *J. Ultrasound Med.*, vol. 22, no.6, pp. 605-623, 2003.
- [77] D. Shen, Y. Zhan and C. Davatzikos, "Segmentation prostate boundaries from ultrasound images using statistical shape model," *IEEE Trans. Med. Imaging*, vol. 22, no.4, pp. 539–551, 2003.
- [78] B. Solaiman, B. Burdsall, C. Roux, "Hough transform and uncertainty handling. Application to circular object detection in ultrasound medical images." *Proceedings 1998 International Conference on Image Processing. ICIP98 (Cat. No.98CB36269). IEEE Comput. Soc.*, vol.3, pp.828-831, Los Alamitos, CA, USA, 1998.
- [79] K. Sutherland, and J.W. Ironside, "Automatic texture segmentation using morphological filtering on images of the human cerebellum," *IEEE Fifth International Conference on Image Processing and its Applications*, pp. 777 – 780, 4-6 Jul 1995.
- [80] K. Valkealathi, and E. Oja, "Reduced Multidimensional Co-Occurrence Histograms in Texture Classification," *IEEE Trans. Pattern Analysis and Machine Intelligence*, vol. 20, no.1, 90-94, 1998.
- [81] D.L. Vilariño, D. Cabello, X. M. Pardo, and V. M. Brea, "Cellular neural networks and active contours: a tool for image segmentation," *Image and Vision Computing* vol. 21, no. 2, pp. 189-204, 10 February 2003.

- [82] J. Weszka, C. Deya, and A. Rosenfeld, "A Comparative Study of Texture Measures for Terrain Classification," *IEEE Trans. System, Man and Cybernetics*, vol. 6, pp. 269-285, 1976.
- [83] K.C. Wong, H.C. Sim, and J. Kittler, "Recognition of two dimensional objects based on a novel generalized Hough transform method," *Proceedings International Conference on Image Processing (Cat. No.95CB35819)*. *IEEE Comput. Soc. Press*, vol.3, pp.376-379, Los Alamitos, CA, USA, 1995.
- [84] R.Y. Wu, K.V. Ling, and W.S. Ng, "Automatic prostate boundary recognition in sonographic images using feature model and genetic algorithm," *J. Ultrasound Med.*, vol. 19, no. 11, pp. 771-782, 2000.
- [85] F. Zana, and J.C. Klein, "Segmentation of vessel-like patterns using mathematical morphology and curvature evaluation," *IEEE Transactions on image processing*, vol. 10, no. 7, pp. 1010 – 1019, July 2001.
- [86] Y. Zhu, S. Williams and R. Zwigelaar, "Computer technology in detection and staging of prostate carcinoma: A review," *Medical Image Analysis*, vol. 10, no. 2, pp. 178-199, April 2006.